

# Observation of the acoustic Purcell effect with a color-center and a nanomechanical resonator

Graham Joe<sup>1\*†</sup>, Michael Haas<sup>1†</sup>, Kazuhiro Kuruma<sup>1,2</sup>,  
Chang Jin<sup>1</sup>, Dongyeon Daniel Kang<sup>3,4</sup>, Sophie W. Ding<sup>1</sup>,  
Cleaven Chia<sup>1,5,6</sup>, Hana Warner<sup>1</sup>, Benjamin Pingault<sup>1,7,8</sup>,  
Bartholomeus Machielse<sup>9</sup>, Srujan Meesala<sup>10</sup>, Marko Lončar<sup>1\*</sup>

<sup>1\*</sup>John A. Paulson School of Engineering and Applied Sciences, Harvard University, 9 Oxford Street, Cambridge, 02138, Massachusetts, USA.

<sup>2</sup>Research Center for Advanced Science and Technology, The University of Tokyo, 4-6-1 Komaba, Meguro-ku, 153-8505, Tokyo, Japan.

<sup>3</sup>Center for Quantum Technology, Korea Institute of Science and Technology (KIST), 5 Hwarang-ro 14-gil, Seongbuk-gu, Seoul, 02792, Republic of Korea.

<sup>4</sup>Division of Quantum Information, KIST School, University of Science and Technology, 5 Hwarang-ro 14-gil, Seongbuk-gu, Seoul, 02792, Republic of Korea.

<sup>5</sup>Quantum Innovation Centre (Q.InC), Agency for Science Technology and Research (A\*STAR), 2 Fusionopolis Way, Innovis # 08-03, Singapore, 138634, Republic of Singapore.

<sup>6</sup>Institute of Materials Research and Engineering (IMRE), Agency for Science Technology and Research (A\*STAR), 2 Fusionopolis Way, #Innovis 08-03, Singapore, 138634, Republic of Singapore.

<sup>7</sup>Center for Molecular Engineering and Materials Science Division, Argonne National Laboratory, 9700 S Cass Ave, Lemont, 60439, Illinois, USA.

<sup>8</sup>Pritzker School of Molecular Engineering, University of Chicago, 5640 S Ellis Ave, Chicago, 60637, Illinois, USA.

<sup>9</sup>Lightsynq Technologies Inc., Boston, 02135, Massachusetts, USA.

<sup>10</sup>Department of Electrical and Computer Engineering, and Smalley-Curl Institute, Rice University, 6100 Main St, Houston, 77005, Texas, USA.

\*Corresponding author(s). E-mail(s): [grj396@g.harvard.edu](mailto:grj396@g.harvard.edu);  
[loncar@g.harvard.edu](mailto:loncar@g.harvard.edu);

†These authors contributed equally to this work.

### Abstract

The radiative properties of atoms are inherently linked to their surrounding environment. Placing an electromagnetic resonator around atoms can enhance spontaneous emission, as shown by Purcell in the 1940s. This approach is now routinely used in quantum computing and communication to channel photons emitted by atoms into well-defined modes and control atom-photon interactions. For solid-state artificial atoms, such as color-centers, the host lattice introduces an acoustic environment, allowing excited atoms to relax by emitting phonons. Here we observe the acoustic Purcell effect by constructing a specially engineered, microwave-frequency nanomechanical resonator around a color-center spin qubit in diamond. Using a co-localized optical mode of the structure that strongly couples to the color-center's excited state, we perform single-photon-level laser spectroscopy at milliKelvin temperatures and observe ten-fold faster spin relaxation when the spin qubit is tuned into resonance with a 12 GHz acoustic mode. Additionally, we use the color-center as an atomic-scale probe to measure the broadband phonon spectrum of the nanostructure up to a frequency of 28 GHz. Our work establishes a new regime of control for quantum defects in solids and paves the way for interconnects between atomic-scale quantum memories and qubits encoded in acoustic and superconducting devices.

**Keywords:** phonons, silicon vacancy, diamond, optomechanics, spin-photon interface, acoustic Purcell effect

## 1 Introduction

It is well-established that an open continuum of electromagnetic modes can cause an excited atom to undergo radiative decay through spontaneous emission [1]. Careful engineering of the electromagnetic environment using cavities and waveguides can be used to control the spontaneous emission rate via the well-known Purcell effect [2, 3]. In cavity quantum electrodynamics (QED) and modern quantum science, this capability is harnessed at the single quantum level to control interactions between atoms and photons [4]. Representative examples include Josephson junction qubits coupled to microwave resonators in superconducting quantum processors [5], atoms and ions in Fabry-Perot cavities [6], solid-state spins in microwave cavities [7], and solid-state optical emitters in nanophotonic devices [8–11] for quantum networking. The physics of an atom in an open continuum also applies to the emission of acoustic waves from an artificial atom in a solid, and is known to limit spin relaxation times in several color-centers [12–15] and rare-earth ion impurities [16, 17] at low temperatures.

Structuring a solid and crafting an acoustic environment with well-defined modes around an atomic-scale impurity could enable quantum acoustodynamics, analogous

to cavity QED with light and microwaves. Phonons in bulk crystalline solids [18, 19] and compact nanomechanical devices [20–22] have been shown to have long lifetimes at milliKelvin temperatures, and can transduce quantum information in various quantum systems including superconducting qubits and photonic devices [23–27]. These prospects have motivated experiments on color-center spin qubits in nanomechanical resonators, including motion-sensing of radio-frequency diamond nanomechanical resonators with nitrogen-vacancy centers [28–31], coherent control of color-center spins with resonant microwave-frequency acoustic waves [32–35], and control of phonon-induced orbital relaxation processes using phononic crystals [36]. A central challenge in this context has been to realize an experimental system that provides high spin-phonon co-operativity, with the threshold for quantum-coherent interactions being unity. In this regime, acoustic radiation from the atomic-scale spin qubit is channeled predominantly into a single acoustic mode relative to the open acoustic continuum. Here we demonstrate such a system by embedding a highly strain-sensitive color-center, the silicon vacancy (SiV) center in diamond [12] in a specially engineered nanomechanical resonator.

We observe the acoustic Purcell effect between the SiV spin qubit and the 12 GHz acoustic mode of the nanomechanical resonator, near its motional ground state at milliKelvin temperatures. The resonator is created in an optomechanical crystal (OMC) [37] that can co-localize photons at the optical frequency linking the spin qubit with the color-center’s excited state. This design provides a minimally invasive window to probe the spin using single-photon-level laser pulses, thereby mitigating laser-induced heating of the acoustic environment at cryogenic temperatures [20, 38]. Simultaneously, the optomechanical crystal allows us to probe the properties of the 12 GHz mechanical mode independent of its interaction with the SiV-center spin. As a further demonstration with our experimental platform, we use optical spectroscopy of the SiV spin qubit to measure the phonon spectrum of the nanostructure over a broad frequency range from 9 to 27 GHz. Our results unlock new possibilities for hybrid quantum systems with color-center quantum memories and fundamental studies of coherence limits in atomic-scale quantum defects.

## 2 Results

The system studied in this work consists of the silicon vacancy (SiV) center, whose optical C transition [39] (Fig. 1c) is coupled to a high quality factor (Q) optical mode of the surrounding OMC resonator (Fig. 1a), while its spin transition simultaneously couples to mechanical modes of the same structure (Fig. 1b). Previous work has demonstrated that an efficient and quantum-coherent spin-photon interface can be realized by integrating SiV centers with optical nanocavities [8]. Furthermore, it has been proposed [12] that an efficient and quantum-coherent spin-phonon interface could be realized by embedding SiV centers within a high-Q and small-mode-volume acoustic cavity [38, 40, 41]. The emitter-optical and spin-mechanical cavity setups, schematically illustrated in Figs. 1a and 1b are realized simultaneously in our experimental system.

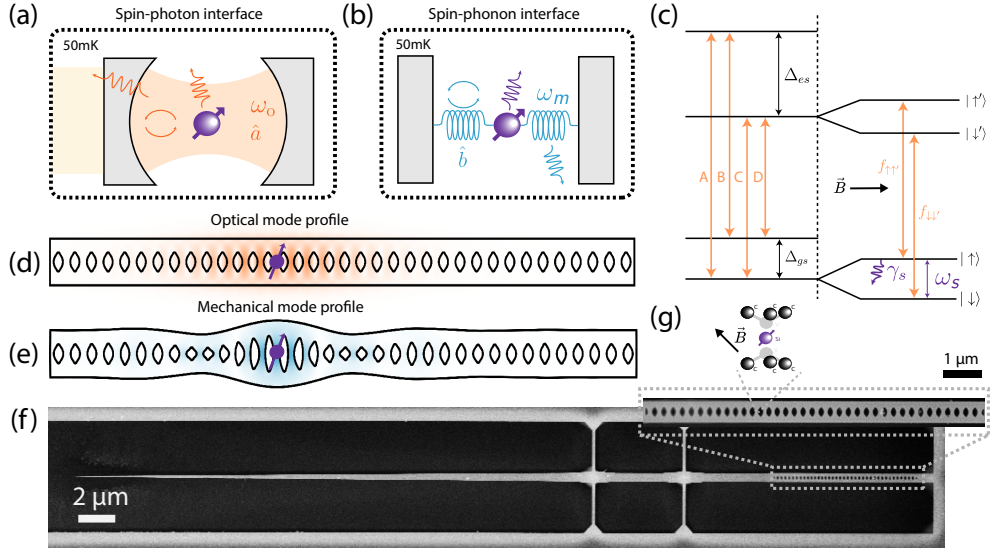


**Fig. 1** Illustration of our experimental system that simultaneously realizes efficient (a) spin-photon interactions, and (b) spin-phonon interactions. The SiV center is embedded in an optomechanical resonator which simultaneously acts as a one-sided optical cavity (orange) with a resonance frequency,  $\omega_o$  and the photon annihilation operator,  $\hat{a}$  and a mechanical resonator (blue) with a resonance frequency,  $\omega_m$  and the phonon annihilation operator,  $\hat{b}$ . (c) Relevant electronic level structure of the SiV center. The splittings between orbital branches in the ground state,  $\Delta_{GS}$  and the excited state,  $\Delta_{ES}$  and the four optical transitions at zero magnetic field A, B, C and D are indicated. The optical cavity frequency,  $\omega_o$  is tuned into resonance with the C-line. An applied magnetic field  $\mathbf{B}$  further splits the energy levels, defining a spin qubit on the lower orbital branch in the ground state with transition frequency  $\omega_s$  which can couple to mechanical modes. Two optical transitions  $f_{\uparrow\uparrow}$  and  $f_{\downarrow\downarrow}$  can be used to initialize and readout the spin qubit's state. (d) Simulated electric field magnitude of the transverse electric (TE)-like optical mode and the approximate location of the implanted SiV center. (e) Simulated strain magnitude (blue) and exaggerated displacement profile of the  $\sim 12$  GHz mechanical breathing mode of the device, with the approximate location of the implanted SiV center. (f) Scanning electron micrograph (SEM) of the device studied in this work: a tapered diamond nanophotonic waveguide on the left is contacted by a tapered optical fiber to couple light in and out of the device. Two sets of tethers are created between widened sections of the diamond waveguide and the bulk diamond substrate for mechanical support and thermal contact. The optomechanical cavity on the far right is shown in detail in the zoomed in SEM in (g), with the molecular structure of the SiV center.

The optical resonator used in this work is single-sided: the mirror on the left of Fig. 1a is less reflective than the mirror on the right such that light can be coupled in and out of the cavity via an optical waveguide mode to maximize photon collection efficiency. The emitter-photon interaction Hamiltonian is given by  $H_{so} = \hbar g_{so}(\hat{a}|e\rangle\langle g| + \hat{a}^\dagger|g\rangle\langle e|)$  where  $g_{so}/(2\pi)$  is the vacuum emitter-photon coupling rate,  $\hat{a}^\dagger$  and  $\hat{a}$  are the intracavity optical mode raising and lowering operators respectively,  $|g\rangle$  is the ground state and  $|e\rangle$  is the excited optical state. The optical cooperativity  $C_o = 4 \frac{g_{so}^2}{\kappa_o \gamma_o}$  is a figure of merit for the spin-photon interface where a value  $C_o > 1$  indicates quantum-coherent spin-photon interactions. Here  $\omega_o/(2\pi)$  is the

frequency of the optical mode,  $\kappa_o/(2\pi)$  is the total loss rate of the optical mode, and  $\gamma_o/(2\pi)$  is the natural linewidth of the emitter. Similarly, the emitter-phonon interaction Hamiltonian is given by  $H_{sm} = \hbar g_{sm}(\hat{b}\hat{\sigma}_+ + \hat{b}^\dagger\hat{\sigma}_-)$  where  $g_{sm}/(2\pi)$  is the vacuum spin-phonon coupling rate,  $\hat{b}^\dagger$  and  $\hat{b}$  are the mechanical mode raising and lowering operators respectively,  $\sigma_+ = |\uparrow\rangle\langle\downarrow|$ , and  $\sigma_- = |\downarrow\rangle\langle\uparrow|$ . We can define  $T_1$ - and  $T_2^*$ -based spin-mechanical cooperativities  $C_{T1} = \frac{4g_{sm}^2}{\kappa_m\gamma_{s,o}}$  and  $C_{T2^*} = \frac{4g_{sm}^2}{\kappa_m\gamma_{s,o}^*}$ . Here  $\omega_m/(2\pi)$  is the frequency of the mechanical mode,  $\kappa_m/(2\pi)$  is the mechanical dissipation rate,  $\omega_s/(2\pi)$  is the spin transition frequency,  $\gamma_{s,o}/(2\pi)$  is the spin relaxation rate into the continuum of the acoustic environment, and  $\gamma_{s,o}^*/(2\pi)$  is the decoherence rate of the spin, including non-Markovian dephasing due to slow magnetic field fluctuations of the nuclear spin environment [42]. Both the optical and mechanical interfaces to the SiV center utilize resonant interactions, enhanced by the simultaneous confinement of photons and phonons in the optomechanical resonator. Crucially, the efficient optical interface to the SiV center allows us to probe and control spin-phonon interactions at the single-photon level, avoiding laser-induced heating at cryogenic temperatures [38, 43], and maintaining the mechanical modes near their quantum ground state.

Our devices consist of a rectangular cross-section diamond waveguide with a one-dimensional array of eye-shaped air holes (5.12). The unit cell dimensions and periodicity of the hole array are chosen to support a simultaneous photonic and phononic bandgap. These devices (Fig. 1f and Fig. 1g) are designed to support a high Q mechanical breathing mode and a high Q optical mode. Fig. 1d and Fig. 1e depict the simulated electric field magnitude for the TE-like optical mode (orange) and simulated strain and deformation profile (blue) for the device's  $\sim 12$  GHz mechanical breathing mode, respectively. Light is coupled into the cavity region via a tapered fiber - diamond waveguide interface [8, 44] (Fig. 1f). The resonant frequency of the optical mode can be frequency-tuned into resonance with the SiV zero-phonon line (ZPL) at 737 nm (406 THz) resulting in an efficient spin-photon interface. This capability enables probing the spin state using ultra-low optical probe powers on the order of 1 pW, thus limiting the laser-induced heating of the mechanical modes that has plagued previous experiments on SiV centers in optomechanical crystals [38]. Due to the significant mode overlap between the TE-like optical mode and the  $\sim 12$  GHz mechanical breathing mode of our device, there is a significant optomechanical coupling (5.6) due primarily to the photoelastic effect [40]. This allows for efficient probing of the properties of the mechanical mode ( $\omega_m, \kappa_m$ ) directly using optomechanical spectroscopy [37, 38, 40], and independently of spin-phonon coupling.

After the fabrication of the diamond optomechanical resonators, which utilizes a quasi-isotropic diamond etch [45] SiV centers are incorporated at the center of the optomechanical resonator by means of masked ion implantation [8, 46]. The implantation dose is chosen to result in 2-3 SiV centers on average per device. SiV centers in the same device are spectrally distinguishable from each other because of variations in the local strain environment of the diamond crystal lattice, which leads to variations in the optical transition frequencies. We address single SiV centers individually in optical frequency space by tuning a laser into resonance with the desired transition.

A simplified diagram of the optical setup used to measure our devices is depicted in Fig. 2a. For single-photon-level optical measurements related to the SiV center, we

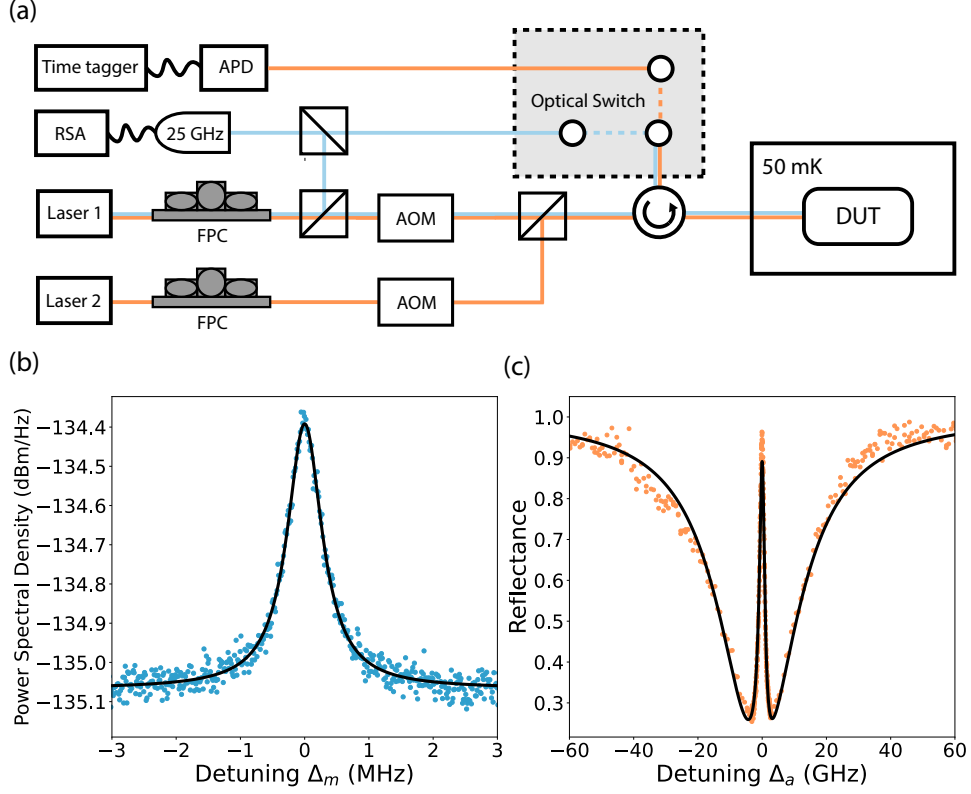


**Fig. 2** (a) Simplified experimental setup diagram. A tunable, continuous-wave laser (Laser 1) is used as a resonant excitation source to optically probe the device. A second laser (Laser 2) can be introduced as needed, and is combined with Laser 1 on a beamsplitter. Laser polarization states are controlled with fiber polarization controllers (FPCs) and the optical pulse sequence is generated using acousto-optic modulators (AOMs). An optical circulator is used to route the light reflected from the device, which is detected either by avalanche photodiode (APD) connected to a time-tagger for photon counting (orange optical path), or by a high bandwidth photodetector (25 GHz) in a heterodyne scheme for optomechanical measurements (blue optical path). (b) Noise power spectral density (NPSD) of thermal motion of the 12.06 GHz mechanical breathing mode of the device measured at 4K at a laser detuning,  $\Delta_o = (\kappa/2)/(2\pi)$  from the optical cavity and at an input optical power of  $50 \mu\text{W}$ . (c) Zero-magnetic-field optical reflection spectrum of the device after the gas condensation frequency tuning procedure, with the SiV C-line on resonance with the optical cavity. A distinct peak in the reflection spectrum can be observed due to hybridization of the optical mode with the SiV C-line. A fit to the optical spectrum allows us to infer the cavity QED parameters of our spin photon interface:  $(g_{so}, \kappa_o, \gamma_o)/(2\pi) = (3.6, 15, 0.11)$  GHz.

use the optical path shown in orange. Two lasers are combined when it is necessary to resonantly address separate optical transitions of the SiV center. Acousto-optic modulators (AOMs) are used to generate optical pulse sequences for spin-decay spectroscopy. For optomechanical measurements performed at comparatively higher laser

power ( $\gtrsim 1 \mu\text{W}$ ), we use the optical path shown in blue. A high bandwidth photodetector (25 GHz) is used in a heterodyne setup for the sensitive detection of mechanical modes of the device with appreciable optomechanical coupling. An optical circulator is used to separate the input and reflected optical fields. We study our devices in a dilution refrigerator setup equipped with a vector magnet, at a base temperature of  $\sim 44 \text{ mK}$  under experimental conditions.

For the device studied in detail in this work, (Fig. 1f and g) we measure a bare optical cavity frequency of  $\omega_o/(2\pi) = 409.7 \text{ THz}$  with an optical Q-factor  $Q_o \approx 27,000$ . We first probe the mechanical breathing mode of the structure via the optomechanical coupling. These measurements are performed at zero magnetic field with the optical transitions of the SiV center far detuned from the optical cavity. Therefore, the SiV does not participate in the optomechanical interaction. The probe laser (frequency  $\omega_l$ ) is detuned by  $\Delta_o = (\omega_l - \omega_o)/(2\pi) = \pm(\kappa_o/2)/(2\pi)$  from the cavity to operate at the maximum optomechanical susceptibility of a sideband-unresolved system [47]. The optically detected noise power spectral density (NPSD) of thermal motion of the mechanical breathing mode at 4K is shown in Fig. 2b. We observe a breathing mode resonance frequency  $\omega_b/(2\pi) = 12.06 \text{ GHz}$  close to the design value, with intrinsic mechanical linewidth  $\kappa_m/(2\pi) \approx 350 \text{ kHz}$  (intrinsic mechanical quality factor  $Q_m \approx 34,000$  measured at 4K) (5.6).

To compensate for the frequency difference between the SiV-center's optical transition and the optical cavity mode, which is caused by finite fabrication tolerances (5.5), we investigated two methods for cavity frequency tuning: in situ gas condensation frequency tuning (gas tuning), and atomic layer deposition (ALD) of alumina (5.3). While the former is commonly used in cryogenic nanophotonic cavity QED experiments [8], the latter technique allowed us to minimize reduction in the Q-factor of the mechanical resonator upon material deposition. The optical Q-factor is not impacted by either tuning method. The optical reflection spectrum of the cavity-SiV system operated on resonance with an input power of  $\sim 1 \text{ pW}$  (intracavity photon number  $\sim 2 \times 10^{-4}$ ) is shown in Fig. 2c. The spectrum features a sharp peak within the cavity dip - a signature of the hybridization between the atomic and optical degrees of freedom [48, 49]. A fit to this spectrum and data at different atom-cavity detunings yields  $(g_{so}, \kappa_o, \gamma_o)/(2\pi) = (3.6, 15, 0.11) \text{ GHz}$  corresponding to an emitter-photon cooperativity of  $C_o = 31$ .

To define a spin qubit with the SiV center, we apply a magnetic field of 2.5 kG along the z- axis in the lab frame ( $\theta \approx 55^\circ$  with respect to the SiV center's high symmetry axis) and lift the spin degeneracy. The frequencies of the Zeeman-split optical transitions, measured via resonant laser excitation spectroscopy, are used to estimate the spin transition frequency,  $\omega_s/(2\pi)$  for any given magnetic field condition (5.1). We initialize the SiV spin state by optically pumping on one of the Zeeman-split transitions. After initializing the spin into the  $|\uparrow\rangle$  state, the population decay rate  $\gamma_s/(2\pi)$  is proportional to the acoustic density of states of the surrounding structure at  $\omega_s/(2\pi)$ . For the range of magnetic fields and the system temperature in these measurements, the spin population is expected to be predominantly in the  $|\downarrow\rangle$  state in the steady state, since  $k_B T \ll \hbar\omega_s$ . In the SI 5.8, we compare spin relaxation measurements performed with optical pumping into the  $|\uparrow\rangle$  and  $|\downarrow\rangle$  states and infer

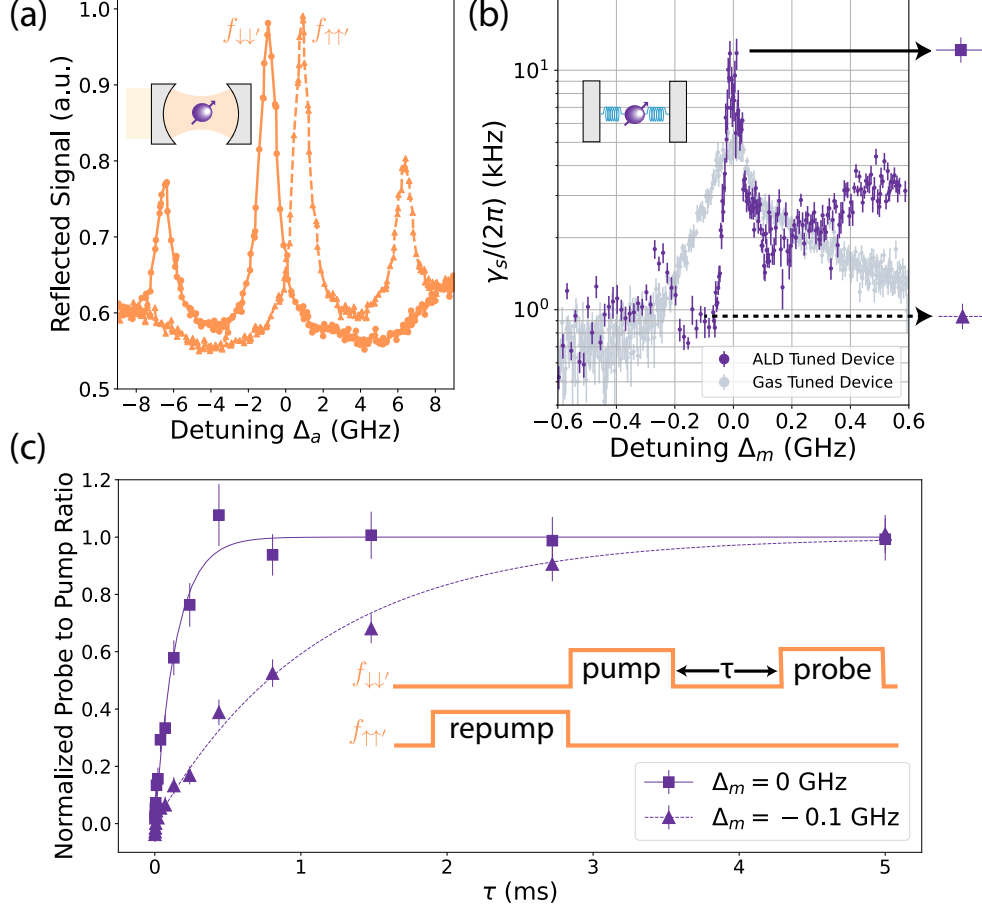


**Fig. 3** (a) Continuous-wave optical reflection spectrum of the spin-photon interface (inset) measured around the SiV center's C-line after the application of a 2.5 kG magnetic field oriented  $\theta \approx 55^\circ$  relative to the SiV center's high-symmetry axis. A repump laser of equal power is resonant with the  $f_{\uparrow\uparrow}$  ( $f_{\downarrow\downarrow}$ ) transition while measuring the spectrum shown with the solid (dashed) trace. The frequencies of the four spin-selective optical transitions of the SiV center's C-line are used to estimate the spin qubit transition frequency  $\omega_s/(2\pi)$  at any given magnetic field condition (5.1). (b) Resonance in the spin decay rate measured when the spin qubit frequency,  $\omega_s/(2\pi)$  is tuned across the  $\sim 12$  GHz breathing mode due to the spin-phonon interaction (inset). The data is taken with a  $\theta \approx 55^\circ$  magnetic field in two separate runs where the optical cavity is tuned into resonance with SiV center's optical transition using the gas tuning method (gray data points), and a combination of ALD and gas tuning (purple data points), resulting in a resonance linewidth of  $\sim 200$  MHz and  $\sim 35$  MHz, respectively. (c) Spin population decay curves for the ALD-tuned device with the spin transition frequency  $\omega_s/(2\pi)$  is at a detuning,  $\Delta_m$  from the  $\sim 12$  GHz mechanical mode of 0 GHz (solid line) and -0.1 GHz (dashed line). (inset) Optical pulse sequence used to measure the SiV center's spin decay rate is shown in the inset of the plot. The repump pulse at the start ensures that the spin qubit is highly polarized into the  $|\downarrow\rangle$  state. The pump pulse then initializes the spin into the  $|\uparrow\rangle$  state. After a controllable delay,  $\tau$  the read pulse is used to read out the population in the  $|\downarrow\rangle$  state relative to the initial fluorescence generated by the pump pulse.

that the SiV environment is at a temperature of  $\sim 150$  mK. At this temperature, the acoustic modes in the environment are close to their quantum ground state, and the  $\sim 12$  GHz breathing mode is expected to have a thermal occupancy of 0.02 quanta.

We studied the SiV center's spin population decay rate,  $\gamma_s/(2\pi)$  as a function of the spin transition frequency,  $\omega_s/(2\pi)$  which is tuned by varying the magnitude of the applied magnetic field. At step changes in the magnetic field, we perform optical spectroscopy to track the optical transition frequencies  $f_{\uparrow\uparrow'}$  and  $f_{\downarrow\downarrow'}$  (5.1). When the detuning between the spin transition frequency and the mechanical breathing mode frequency  $\Delta_m = (\omega_s - \omega_b)/(2\pi)$  approaches zero, a distinct peak in the spin population decay rate is observed, as shown in Fig. 3b, indicating a Purcell enhancement of the spin relaxation rate. The gray data points depict data observed when the optical cavity frequency tuning is performed in situ using the gas condensation method to shift the optical resonance from 409.7 to 406.7 THz. This approach results in a broad resonance in the Purcell-enhanced spin relaxation rate with a linewidth of  $\sim 200$  MHz. On the other hand, the purple data points are obtained after conformal deposition of  $\sim 5$  nm of alumina using ALD to shift the optical resonance from 409.7 THz to 406.9 THz, followed by in-situ gas tuning to shift the optical resonance to 406.7 THz. This approach results in a linewidth of  $\sim 35$  MHz for the Purcell enhancement. In the former case, the measured linewidth is a factor of 500 larger than the intrinsic mechanical linewidth of 350 kHz measured via optomechanics (5.6). To further investigate the significant difference in the linewidth of the Purcell enhancement observed between both cavity-tuning methods, we performed optomechanical spectroscopy on the device after ALD alumina deposition. As described previously for the data presented in Fig. 2(b), this measurement is independent of the SiV center. We observe that the deposition of the ALD alumina layer broadens the intrinsic mechanical linewidth to 650 kHz (5.6). In our experimental setup, such an independent optomechanical spectroscopy measurement cannot be performed on a gas-tuned device because the requisite optical powers ( $\sim 1$   $\mu$ W) boil off the condensed gas. Nonetheless, this combination of spin-relaxation and optomechanical measurements indicates that the amount of gas condensed on the device is strongly correlated with the linewidth of the Purcell enhancement in Fig. 3b due to the mechanical resonator. Since the ice deposited on the structure due to gas condensation is expected to have significantly lower speed of sound relative to diamond [50], we expect gas condensation to increase acoustic radiative loss from the mechanical resonator into the bulk substrate, introducing excess damping.

For the remainder of the discussion, we present data measured on the device using the ALD cavity-tuning method and minimal residual gas condensation, with corresponding data for the gas-tuning method shown in the SI 5.3. Fig. 3c shows the spin population decay curves measured at zero detuning from the breathing mode (solid curve) and with a detuning of -0.1 GHz, clearly illustrating the Purcell enhancement in spin relaxation between the on and off-resonant cases. The optical pulse sequence used to measure the SiV center's spin population decay rate at a given spin transition frequency  $\omega_s/(2\pi)$  is shown in the inset. A repump laser excites the  $f_{\uparrow\uparrow'}$  ( $f_{\downarrow\downarrow'}$ ) transition while a pump/probe laser tracks the  $f_{\downarrow\downarrow'}$  ( $f_{\uparrow\uparrow'}$ ). When the time delay  $\tau$  between the pump and probe pulses is increased, the SiV center's spin population read out using

the probe decays towards its thermal equilibrium value. The data fits well to an exponential decay, allowing us to extract the spin relaxation rate. The Purcell-enhanced spin-decay rate due to a near ground state mechanical resonance where  $\kappa_m \gg \gamma_s$  is given by  $\gamma_s = \gamma_{s,o} + g_{sm}^2 \frac{\kappa_m}{\kappa_m^2/4 + (\omega_s - \omega_b)^2}$  where  $\gamma_{s,o}$  is the spin relaxation due to the environment of the spin mechanical resonator system. We measure  $\gamma_s/(2\pi) \approx 1$  kHz at a detuning of -0.1 GHz from the resonance which we take as the value of  $\gamma_{s,o}/(2\pi)$ , and we measure  $\gamma_s/(2\pi) \approx 10$  kHz on resonance. With the linewidth of the resonance measured as  $\kappa_m/(2\pi) = 35$  MHz, we infer a spin-phonon coupling rate of  $g_{sm}/(2\pi) \approx 300$  kHz. Our simulations suggest that under ideal conditions of low static strain and accurate SiV placement at the breathing mode strain maximum,  $g_{sm}/(2\pi)$  could attain a maximum value of 9 MHz (5.13). The difference between this maximum value and the experimentally measured value is well explained by the non-ideal conditions in the studied device, including the presence of static strain (5.2) and the typical expected error in SiV placement. Our measurements correspond to a  $T_1$ -based cooperativity  $C_{T_1} \approx 10$ . Assuming the previously measured value for the SiV center spin linewidth,  $\gamma_{s,o}^*/(2\pi) \approx 1$  MHz [8] in photonic crystal cavities with similar dimensions, this corresponds to a  $T_2^*$ -based cooperativity  $C_{T_2^*} \approx 0.01$ .

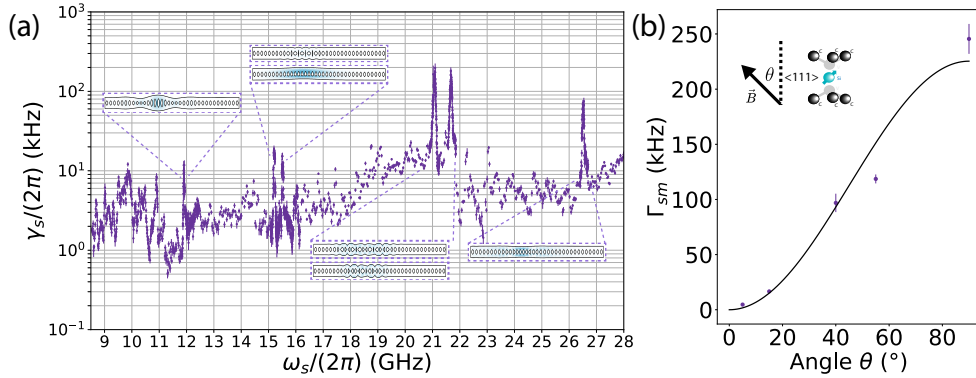


**Fig. 4** (a) Broadband spectrum of the spin decay rate,  $\gamma_s$  for a  $\theta \approx 55^\circ$  magnetic field. Several resonances in addition to the  $\sim 12$  GHz breathing mode are observed and attributed to other mechanical modes of the device (insets), as confirmed by numerical simulations (5.12). (b) Dependence of the spin decay rate on the angle of the applied magnetic field relative to the SiV center's symmetry axis measured on the mechanical resonance at  $\sim 21$  GHz. The solid line is a single-parameter fit to the relation,  $\Gamma_{sm} = A \sin^2 \theta$ , the theoretical dependence expected from the SiV spin-strain interaction Hamiltonian [12].

In addition to the resonance induced by the mechanical breathing mode, several distinct features are observed in the spin decay spectrum of Fig. 4a. This broadband spectrum is taken with a  $\theta \approx 55^\circ$  aligned magnetic field. We attribute these resonances in the spin decay rate to other localized mechanical modes of the nanostructure with appreciable spin-phonon coupling to the SiV. Although these modes cannot be observed independently using optomechanical spectroscopy, numerical simulations of

the acoustic mode structure of our device reveal several acoustic modes with appreciable spin-phonon coupling and negligible optomechanical coupling. This is because while the former simply requires an appreciable strain amplitude due to the mode at the SiV-center’s location, the latter requires an appreciable value for the photoelastic overlap integral between the optical and mechanical mode profiles extending over the volume of the structure. We find that our numerical simulations can reproduce the overall qualitative shape of the experimentally measured spin decay spectrum (5.14), confirming that our spin relaxation spectroscopy technique can detect phonon modes of the nanostructure beyond the resonances with appreciable optomechanical interactions (5.12). However, the precise frequencies of acoustic resonances detected (besides the breathing mode) and the corresponding magnitudes of Purcell enhancement are strongly dependent on the position of the SiV center within the OMC device (see supplementary information 5.13).

To further confirm the acoustic origin of the Purcell enhancement, we measure the dependence of the spin relaxation rate on the orientation of the magnetic field. Based on theoretical predictions using the SiV strain interaction Hamiltonian [12], the magnitude of Purcell-enhanced spin decay rate ( $\Gamma_{sm} = \gamma_{s,\omega_m} - \gamma_{s,o}$ ) should increase as the magnetic field vector rotates away from the SiV center’s high-symmetry axis towards the plane perpendicular to that axis due to increased mixing between the spin-orbit eigenstates. Since the splitting between the  $f_{\uparrow\uparrow}$  and  $f_{\downarrow\downarrow}$  transitions is relatively small when the magnetic field is nearly aligned with the SiV axis, we performed this angle-dependence measurement on a higher frequency acoustic resonance of the device at  $\sim 21$  GHz. Using the vector magnet in our experimental setup, we sweep the spin transition frequency across this resonance using the magnetic field magnitude for five different magnetic field orientations (5.10). Following the standard cavity QED framework for the Purcell effect [1], we expect  $\Gamma_{sm} \propto g_{sm}^2$ . Further, the Hamiltonian of the SiV center dictates that the acoustic dipole moment (strain susceptibility) for the spin qubit, and hence  $g_{sm}$  is proportional to the component of magnetic field perpendicular to the SiV-center’s high-symmetry axis [12]. In Fig. 4b, the fit to the data indicates good agreement with this  $\sin^2\theta$  dependence expected from theory.

### 3 Conclusions and Outlook

In conclusion, we observed the acoustic Purcell effect between a single color-center spin qubit and a nanomechanical resonator. We demonstrated sensing of the broadband phonon spectrum of the nanostructure using the color-center as an atomic-scale acoustic probe. At the 12-GHz acoustic resonance of the device, we observe a Purcell enhancement or  $T_1$ -based spin-phonon cooperativity,  $C_{T_1} \approx 10$  and a  $T_2^*$ -based cooperativity,  $C_{T_2^*} \approx 0.01$ . While this is the highest spin-phonon cooperativity observed to date, we expect future advances in our experimental platform to enable  $C_{T_2^*} > 1$ , the regime for most applications involving quantum-coherent interactions. In the present work, the cooperativity is primarily limited by excess mechanical damping (increased  $\kappa_m$ ) from the material deposition (gas condensation or ALD alumina) required to tune the co-localized optical mode into resonance with the SiV. An increase in cooperativity of at least two orders of magnitude is feasible with tuning methods that

avoid material deposition, such as electrostatically-tunable zipper cavities [51]. In this regime, the system can be used to perform bi-directional transduction of quantum states between the spin qubit and the acoustic mode. The acoustic resonator in our platform is amenable to co-design with recently developed electro-optomechanical [21] and piezo-optomechanical quantum transducers [24, 27, 52], strengthening prospects for interconnecting color-center spin-based quantum memories with superconducting qubits[53]. Such a hybrid quantum system would combine the exceptional coherence and atomic-scale footprint of color-center spin qubits with fast, high-fidelity superconducting qubit gates, and provide unique opportunities for next-generation quantum networks [54] and distributed quantum information processing [55].

Beyond applications involving hybrid quantum hardware, we expect the spin-phonon cooperativity can be further boosted by reducing acoustic radiative loss into the continuum through phononic bandgap shielding, previously used to achieve ultra-high-Q GHz-frequency, nanoscale acoustic resonators in silicon [20]. In this setting, our system will enable the realization of acoustic metamaterials with strong atom-phonon interactions and chip-scale quantum networks [56, 57] as well as fundamental studies of materials noise with phonon-engineered two-level-system defects [58–60].

### 3.1 Data Availability

The data that support the findings in this study are available from the authors on reasonable request.

## 4 Acknowledgments

The authors would like to thank M. Bhaskar, D. Assumpcao, and C. Knaut for fruitful discussions. This research was supported by the National Science Foundation under grant number DMR-1231319, titled “Center for Integrated Quantum Systems (CIQM),” the Army Research Office/Department of the Army under award number W911NF1810432, titles “Ab-Initio Solid-State Quantum Materials: Design, Production, and Characterization at the Atomic Scale,” the Office of Naval Research under award number N00014-20-1-2425, titled “Quantum Information Processing With Phonons,” the National Science Foundation under award number EEC-1941583, titled “NSF Engineering Research Center for Quantum Networks (CQN),” the Air Force Office of Scientific Research under award number FA9550-23-1-0333, titled “Quantum Phononics to Advance Quantum Information Processing,” the National Research Foundation funded by the Korean government (NRF-2022M3K4A1094782), and Amazon Web Services under award number A50791, titled “Partnership for Quantum Networking.” G. J was supported in part by the Natural Sciences and Research Council of Canada (NSERC). K.K. acknowledges financial support from JSPS Overseas Research Fellowships (Project No. 202160592). This work was partly supported by the KIST institutional program (2E33541, 2E33571) funded by the Korea Institute of Science and Technology, and the National Research Foundation of Korea (NRF) grant (No. RS-2022-NR068818), funded by the Korean government (MSIT). C. C was supported in part by Singapore’s Agency for Science, Technology and Research (A\*STAR). H. W acknowledges financial support from the NSF GRFP fellowship. B.

P. acknowledges financial support from Q-NEXT, a U.S. Department of Energy Office of Science National Quantum Information Science Research Centers under award number DE-FOA-000225. B.M. is involved in developing diamond photonic technology at Lightsynq Technologies Inc. This work was performed in part at the Center for Nanoscale Systems (CNS), a member of the National Nanotechnology Infrastructure Network (NNIN), which is supported by the National Science Foundation award ECS-0335765. CNS is part of Harvard University.

## 5 Supplementary information

### 5.1 Calibration of Spin Transition Frequency

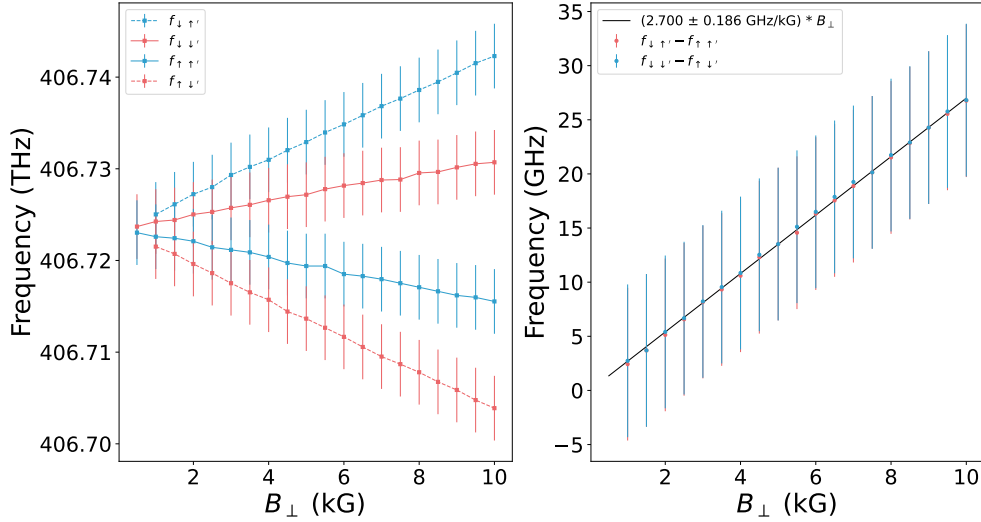


**Fig. 5** Calibration of the spin transition frequency versus applied magnetic field. (a) For any given magnetic field orientation, (in this case perpendicular to the SiV center's symmetry axis), the spin-selective optical transitions shift linearly as a function of the applied field magnitude. (b) The spin transition frequency can be estimated from  $f_{\downarrow\uparrow'} - f_{\uparrow\uparrow'}$  and from  $f_{\downarrow\downarrow'} - f_{\uparrow\downarrow'}$ . A linear fit with zero y-intercept to these estimates yields a conversion factor between the magnetic field magnitude and the spin transition frequency (in this case, 2.7 GHz/kG).

The spin-selective optical transition frequencies depicted in Fig. 2a shift linearly as a function of the magnitude of the applied magnetic field. Specifically, both  $f_{\downarrow\uparrow'} - f_{\uparrow\uparrow'}$  and  $f_{\downarrow\downarrow'} - f_{\uparrow\downarrow'}$  allow us to estimate  $\omega_s/(2\pi)$ . Here  $f_{\uparrow\uparrow'}$  and  $f_{\downarrow\downarrow'}$  are as shown in Fig. 1c.  $f_{\downarrow\uparrow'}$  is the optical transition between the  $|\downarrow\rangle$  and the  $|\uparrow'\rangle$  state (the leftmost line in Fig. 3a) and  $f_{\uparrow\downarrow'}$  is the optical transition between the  $|\uparrow\rangle$  and the  $|\downarrow'\rangle$  state (the rightmost line in Fig. 3a). The optical transitions have a maximum Purcell enhanced linewidth of 3.5 GHz, which practically eliminates the effects of spectral diffusion on our experiment. For any given magnetic field orientation, a linear fit to the estimated

spin transition frequency at several calibration field magnitudes yields a conversion constant between applied field magnitude and spin transition frequency. In the case of a perpendicular field shown in Fig. 5, we get a conversion constant of  $2.700 \pm 0.186$  GHz/kG.

For our spin decay spectroscopy measurements, we use the  $f_{\uparrow\uparrow'}$  and  $f_{\downarrow\downarrow'}$  transitions because of their large photon scattering rate and comparatively small movement as a function of the applied magnetic field magnitude. The value of the conversion constant depends on the angle of the applied magnetic field and is calibrated at every angle for the angle-dependent measurements in Fig. 4. In particular, for a given field magnitude, a magnetic field oriented perpendicular to the SiV center's symmetry axis will produce the minimum spin transition frequency, whereas a field aligned with the symmetry axis will produce the maximum spin transition frequency. The value of the conversion constant also depends on the static crystal strain experienced by the SiV center, which can be inferred from the ground state orbital splitting [12]. It was observed to change after ALD alumina cladding 5.2, and to a lesser extent after repeated gas tuning. Therefore, this calibration curve is retaken after any material deposition performed to tune the optical resonance.

## 5.2 Measurement of SiV Static Strain Environment

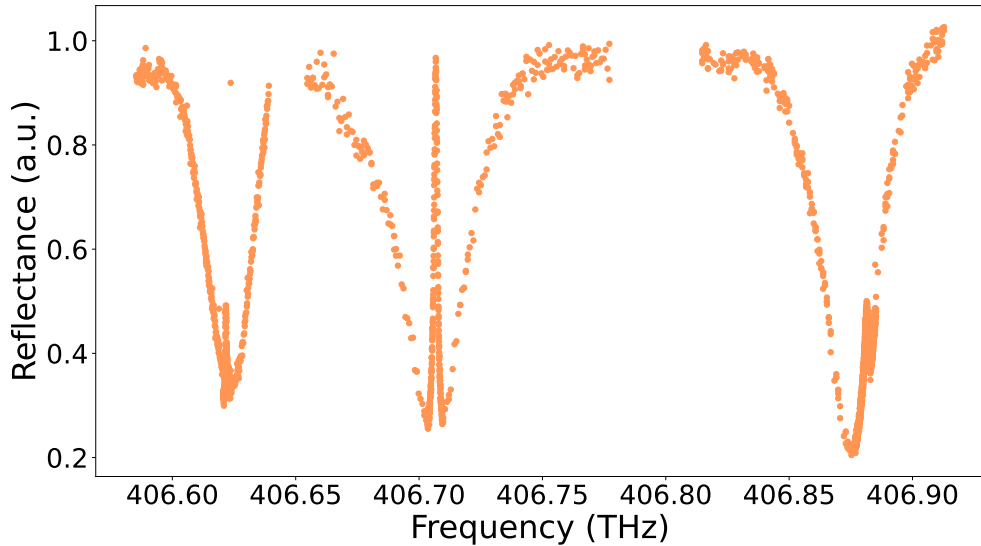


**Fig. 6** Optical reflection spectrum of the SiV cavity system with the optical cavity (broader feature) gas tuned into resonance with the D (left), C (middle), and B (right) optical transitions in the SiV fine structure. From the measured optical transition frequencies we infer a ground state splitting  $\Delta_{GS} = 85$  GHz and an excited state splitting  $\Delta_{ES} = 260$  GHz corresponding to a moderately strained SiV center.

Using the gas tuning capabilities of our experiment, it is possible to tune the optical resonance of the TE-like optical mode of our devices into resonance with each of the lines in the fine structure of an optically coupled SiV center’s ZPL [39]. These measurements are performed at zero magnetic field. At  $\sim 4\text{K}$ , a distinct narrow resonance within the optical reflection spectrum is observed at the frequency resonant with the atomic line [48, 49]. Knowledge of the frequency splittings of an SiV center’s fine structure is useful because it can be used as a measurement of the static crystal strain experienced by the SiV center. The data in Fig. 6 was taken after the device was cladding in ALD alumina making it impossible to reach the bluest transition (the A-line). However, the observation of three lines is sufficient to measure the ground and excited state splittings ( $\Delta_{GS} = 85\text{ GHz}$  and  $\Delta_{ES} = 260\text{ GHz}$  respectively). Note that at millikelvin temperatures where the ground state phonon transition is frozen out, the B and D line go dark due to a lack of population in the upper branch of the ground state, making them unsuitable for measurements in this temperature range.

### 5.3 Gas Tuning and ALD Cladding

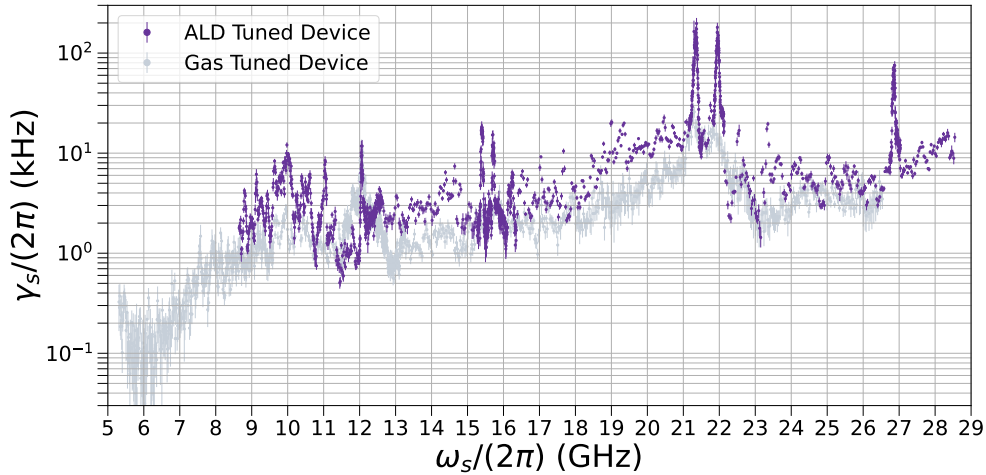


**Fig. 7** Comparison between the broadband spin decay spectra when the optical mode of the device is tuned entirely via gas condensation with a  $\theta \approx 55^\circ$  B-field orientation (gray) and mostly via ALD alumina cladding with minimal gas condensation with a  $\theta \approx 90^\circ$  B-field orientation (purple).

The optical mode of our device can be tuned into resonance with the SiV center’s C-line by in-situ gas condensation. Gas is delivered to the sample through a copper tube thermally connected to the 4K plate of the dilution refrigerator. This tube inside the fridge is mated to a stainless steel tube which runs outside of the fridge. Resistive heaters and dedicated thermometers are installed on the gas tube, allowing control of the tube temperature. During the cooldown, after the fridge reaches a temperature of about 4K, the tube is heated above the boiling temperature of inert gases, which

can then condense on the sample. We observed that once the gas tube reaches a temperature in the range of 35-45K, the optical resonance of our device begins to red-shift, indicating gas condensation. Using this method, we achieve a coarse wavelength shift of the cavity resonance to a longer wavelength with respect to the SiV C line. After this step, a fine-tuning step is performed to blue-shift the cavity resonance onto the SiV C line. This is achieved via controlled boiling of the condensed gas with a high-power broadband laser (NKT Photonics, Super K supercontinuum white light laser) through the tapered fiber interface, which blue-shifts the resonance. During this tuning process, the optical resonance frequency is monitored in real time on a spectrometer (Princeton Instruments HRS-750).

To further study the effect of gas condensation, we also studied these devices with minimal gas condensation by cladding the devices in  $\sim 5$  nm of alumina by atomic layer deposition (ALD). Following deposition, sample mounting and cool-down, the optical mode of this device was 736.8 nm (406.825 THz), and the intrinsic mechanical linewidth broadened to 650 kHz. Note that thermorefractive shifts and potential residual condensation of material on the device during cool-down can slightly shift the resonance frequency relative to the ambient room temperature case. Further gas condensation was required to achieve resonance with the SiV center's C-line, but a comparatively small amount relative to the bare device. The gray trace in Fig. 7 corresponds with the case where the optical cavity was tuned entirely by gas condensation and the magnetic field alignment of  $\theta \approx 90^\circ$ , while the purple trace corresponds to the case of ALD alumina cladding with minimal gas condensation and the magnetic field alignment of  $\theta \approx 55^\circ$ . However, as shown in the angle-dependent measurements in Fig. 15, the angle of the applied magnetic field has negligible effect on the linewidth of the Purcell enhancement due to an acoustic resonance. In both spectra, a distinct peak is observed around 12 GHz where the mechanical breathing mode is expected. The linewidth of this feature is substantially broadened in the gas-tuned device related to the ALD-tuned device. In addition to the  $\sim 12$  GHz feature shown in Fig. 3a, several other features in the spin decay spectrum were observed to narrow in linewidth with some features becoming visible that were previously not apparent in the fully gas tuned spectrum. We attribute these features to other mechanical modes of the structure, which are not observed in the optomechanically transduced noise power spectrum measurements because of insufficient optomechanical coupling (5.12).

## 5.4 Measurement Setup

Our measurement setup is designed to enable both SiV spectroscopy and optomechanical measurements in slightly different configurations. SiV measurements require low input laser powers on the order of 1 pW at the device, while optomechanical measurements require input powers at the device on the order of 1  $\mu$ W or more.

The primary laser used in our experiments for resonant optical excitation of SiVs is a continuous-wave Ti:Sapphire laser (MSquared, Laser 2 in Fig. 8). SiV measurements sometimes require a repump laser (Toptica DL Pro, Laser 1 in Fig. 8). Optomechanical measurements use power split off from Laser 2 as a reference local oscillator (LO) in a heterodyne scheme. We use the upper branch of the laser preparation path for optical power measurement and control. An optical switch (Photonwares) is used to direct

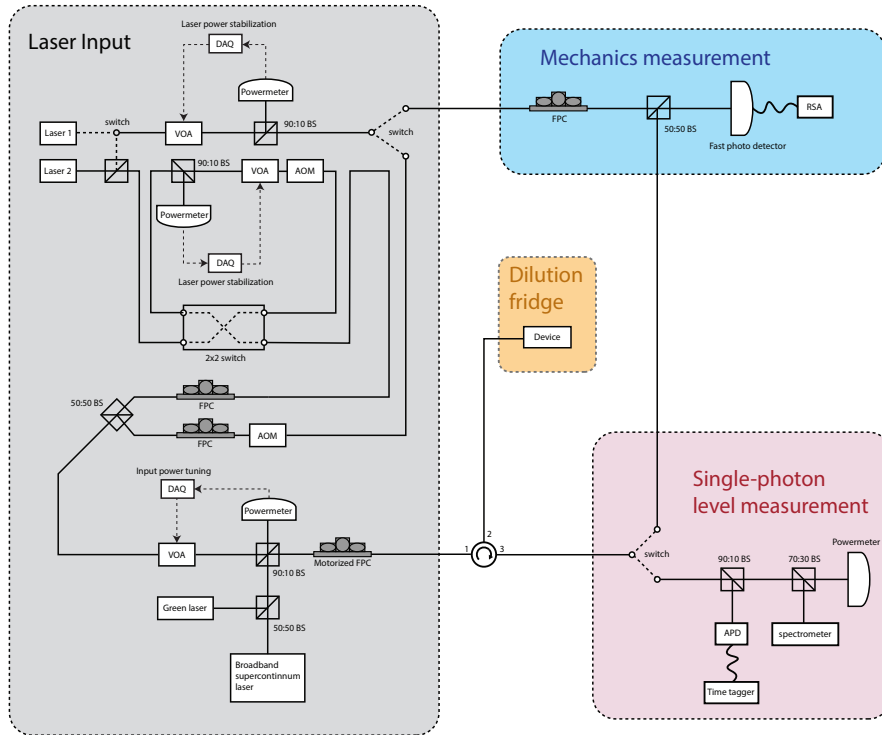


**Fig. 8** Schematic of measurement setup. VOA: Variable Optical Attenuator, BS: Beamsplitter, DAQ: Data Acquisition Device, AOM: Acousto-Optic Modulator, FPC: Fiber Polarization Controller, APD: Avalanche Photodetector.

the laser towards the sample for SiV measurements and towards a high bandwidth photodetector (Thorlabs, RXM25DF) for use as an LO in the heterodyne scheme for optomechanical measurements.

On both the upper and lower branches of the resonant laser input path, we use a voltage-controlled variable optical attenuator (Thorlabs VOA, 0-5 V) followed by a 90:10 fiber beamsplitter with a powermeter (Thorlabs) on the 10% port for setting and locking the input power, if desired. An analog output voltage from the powermeter is measured with a data acquisition device (DAQ, National Instruments NI-USB 6363) and the input power can be locked with a PID loop. Prior to combination of the resonant laser paths on a 50:50 beamsplitter, both lasers pass through a fiber acousto-optic modulator (AOM, AA Optoelectronics MT200-R18-Fio-PM-J1-A-VSF) and a manual fiber polarization controller (FPC) which can set the relative polarization of the lasers. Each AOM is driven by a 200 MHz source which is in turn controlled by a microwave switch followed by a microwave amplifier. The microwave switch is controlled by a

delay generator (Stanford Research Systems DG645). After being combined, the resonant lasers pass through a second voltage controlled VOA. Combined with the first VOA, this allows for the required  $\sim 60$  dB of dynamic range in power control for locking of the input power while achieving picoWatt-level powers at the device. On Laser 2's path, we add a 2x2 optical switch which can bypass the VOA and AOM. This is used to reduce optical path loss during optomechanical heterodyne measurements. In this case, the VOA and power meter further downstream can be used to control the power of Laser 2.

The resonant input lasers are finally combined with a green diode laser (Thorlabs DJ532-10) and a broadband super-continuum laser (NKT Photonics SuperK EXTREME) on a 2x2 fiber beamsplitter. The green laser is used for charge state repumping. The broadband laser is used for low-resolution reflection measurements in combination with a spectrometer (Princeton Instruments, HRS-750) and for fine frequency adjustment of gas-tuned OMC devices. The unused port of the 2x2 beamsplitter can be used for input power measurements. A motorized fiber polarization controller is used for automated control of the input laser polarization state during long measurements.

A fiber optic circulator customized for operation at 737 nm (Ascentta Optics) is used just before the input to the dilution fridge (Bluefors LD250) to separate the device reflection from the input with a low insertion loss of about 1 dB per pass. The optical fiber going to the device is routed through a blank KF flange with a small hole drilled through the middle, which is then sealed shut with Torr Seal. The fiber runs down the length of the fridge, and is looped and taped to the mixing plate in an attempt to thermalize the fiber to the mixing plate as well as possible before reaching the device. The fiber is then spliced to a tapered optical fiber mounted on a stack of three Attocube stages (ANPxz101/LT/HV), used for positioning the fiber relative to the sample. The base temperature of our fridge under experimental conditions is  $\sim 44$  mK.

Reflection from the device can then be directed either to single-photon-level detection paths where we perform optical characterization of our devices and all SiV-related measurements, or to an optomechanical measurement path. The main detector used in for single-photon level measurements in this work is an APD (Perkin Elmer) connected to a Time-Tagger (Swabian). We use a powermeter (Thorlabs, PM101A) for higher power measurements, and a spectrometer (Princeton Instruments, HRS-750) for low-resolution reflection measurements (5 GHz resolution, allows for live reflection spectrum monitoring e.g. during gas tuning) and fluorescence measurements.

For optomechanical measurements, device reflection is combined with an LO derived from the original laser on a 2x2 fiber 50:50 beamsplitter. The polarization of the LO is matched to the device reflection using an FPC. One output port of the 2x2 beamsplitter is not used while the other goes to a high-bandwidth silicon photodetector (Thorlabs, RXM25DF) connected to a real-time spectrum analyzer (RSA, Tektronix 5126A). Modulation of the laser reflected from the device due to mechanical modes with significant optomechanical coupling generates optical side-bands, which beat with the LO and generate a microwave frequency voltage signal that is detected on the RSA.

## 5.5 Fabrication of Rectangular Cross-Section SiV-OMC Devices

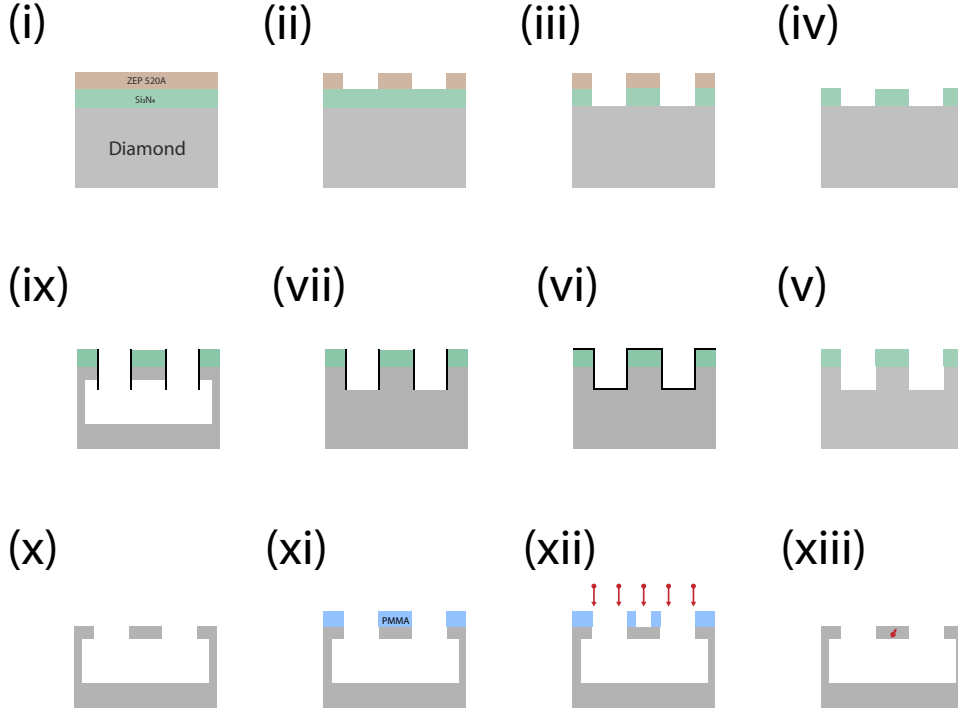


**Fig. 9** Schematic of process flow for the SiV-OMC device fabrication. The OMC devices are fabricated in diamond based on a quasi-isotropic etching technique (i-x). The SiV centers are deterministically generated and incorporated into the fabricated OMC devices by masked ion implantation process (x-xiii). This procedure typically results in a few SiV centers per cavity, the device studied in this work had a single detectable SiV center.

The rectangular cross-section SiV-OMC devices are fabricated by quasi-isotropic etching. [38, 45, 61] An overview of the fabrication process is shown in Fig. 10. We use plasma-enhanced chemical vapor deposition to make a 100 nm-thick SiN layer on the bulk diamond before spin-coating a 400 nm-thick electron beam (EB) resist (ZEP 520A) [(Fig. 9(i))]. The OMC pattern is created on the EB resist by EB lithography and resist development [(Fig. 9(ii))]. The SiN layer is etched by inductively coupled plasma-reactive ion etching (ICP-RIE) [(Fig. 9(iii))]. After the EB resist is removed[(Fig. 9(iv))], the OMC pattern is transferred into the diamond by oxygen plasma RIE[(Fig. 9(v))]. We deposit 20 nm-thick Al<sub>2</sub>O<sub>3</sub> by atomic layer deposition (ALD) for conformal coverage of the sample[(Fig. 9(vi))]. We etch the Al<sub>2</sub>O<sub>3</sub> layer by RIE with Ar and Cl gases, maintaining the sidewalls of the OMC devices covered with

$\text{Al}_2\text{O}_3$  [(Fig. 9(vii))]. We realize the free-standing structures using the quasi-isotropic etching technique based on an oxygen-based RIE[(Fig. 9(ix))]. We remove the  $\text{Al}_2\text{O}_3$  and SiN layers by hydrofluoric acid.

To implant SiV centers in the fabricated OMC devices, we spin-coat a PMMA layer on the fabricated devices [(Fig. 9(xi))] and create the mask for the deterministic ion implantation process. After masked ion implantation [(Fig. 9(xii))], we remove the PMMA layer to complete the fabrication of OMC devices [(Fig. 9(xiii))]. The SiV centers in OMC devices are generated by annealing. The details of the mask ion implantation technique can be found in our previous report[62]. We note that our fabricated devices typically have a few SiV centers, we use an OMC device with a single SiV center in this work.

## 5.6 Power Dependent Mechanical Linewidth

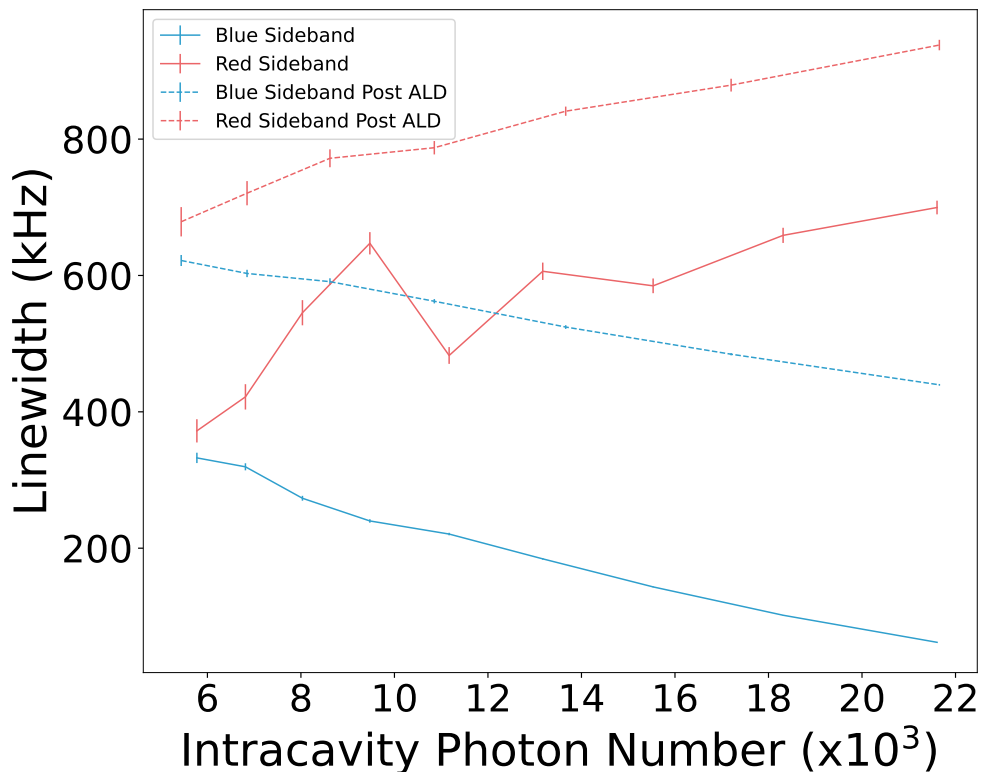


**Fig. 10** Power dependent mechanical mode linewidth with laser parked on the red (blue) sideband for the red (blue) trace before (after) ALD alumina cladding is show with the solid (dashed) lines. Extrapolated intersection of the red/blue sideband curves yield an intrinsic mechanical linewidth of  $\sim 350$  kHz ( $\sim 650$  kHz) before (after) ALD alumina cladding.

With sufficiently large input power, the effects of optomechanical backaction can become significant relative to the intrinsic mechanical linewidth of the mechanical mode. Our devices are in the sideband unresolved regime where  $\omega_m < \kappa$ , so we use an optical probe detuning of  $\Delta = \pm\kappa/2$  to measure the blue (red) sideband optical power dependence of the mechanical mode linewidth. On the blue sideband, optomechanical backaction counteracts the intrinsic damping mechanisms thereby narrowing the mechanical linewidth towards zero (the phonon lasing threshold), whereas on the red sideband the optomechanical backaction further damps the mechanical mode. The slope of the curves in Fig. 10 are related to the optomechanical coupling rate while the y-intercept is the intrinsic mechanical dissipation rate. The solid traces in the lower part of the plot correspond to the bare device, while the dashed traces in the upper part of the plot correspond to the same device after cladding in ALD alumina.

An increase in intrinsic linewidth from  $\sim 350$  kHz to  $\sim 650$  kHz is observed following the cladding of the OMC in alumina. Both of these values are two to three orders of magnitude narrower than the corresponding  $\sim 12$  GHz frequency feature observed in the spin decay spectrum measurement in Fig. 3. We attribute this difference to excess mechanical dissipation introduced by the gas condensation procedure required to achieve the optical resonance condition between the TE-like optical mode and the SiV center's ZPL.

## 5.7 Raw Data for Spin Relaxation Measurements

An example histogram of the photon counts measured by the APD connected to the time-tagger for a particular time delay  $\tau$  of the optical pulse sequence is shown in Fig. 11. The initialization peak seen at the beginning of each pulse corresponds to a short time of increased reflection from the device as the spin is pumped to the opposite state (shaded). The repump pulse at the beginning of the sequence, which is resonant with the  $f_{\uparrow\uparrow}$  transition, is intended to ensure that the spin population begins predominantly in the  $|\downarrow\rangle$  state. Following this repump pulse, the pump and probe pulses are resonant with the  $f_{\downarrow\downarrow}$  transition. The pump pulse then pumps the spin population into the  $|\uparrow\rangle$  state and produces an initial peak fluorescence corresponding to maximum population in the  $|\uparrow\rangle$  state. After the variable wait time  $\tau$ , the height of the initial fluorescence signal on the probe pulse relative to the height of the initialization peak on the pump pulse is a measurement of the fraction of the population that has relaxed into the  $|\downarrow\rangle$  state. The  $f_{\uparrow\uparrow}$  and  $f_{\downarrow\downarrow}$  are nominally spin-conserving transitions, but in a magnetic field not aligned with the SiV center symmetry axis, this spin selection rule is relaxed and the transitions can be used to polarize the spin. In some of our spin relaxation measurements, we found that the repump pulse does not completely polarize the spin population with the maximum fidelity, however the timescale of the spin relaxation, which is the quantity of interest in our measurements, is unaffected.

## 5.8 Temperature-Dependent Spin Decay

We performed thermometry measurements by probing the SiV center spin relaxation with low input laser powers on the order of 1 pW. The measurement in Fig. 12 shows

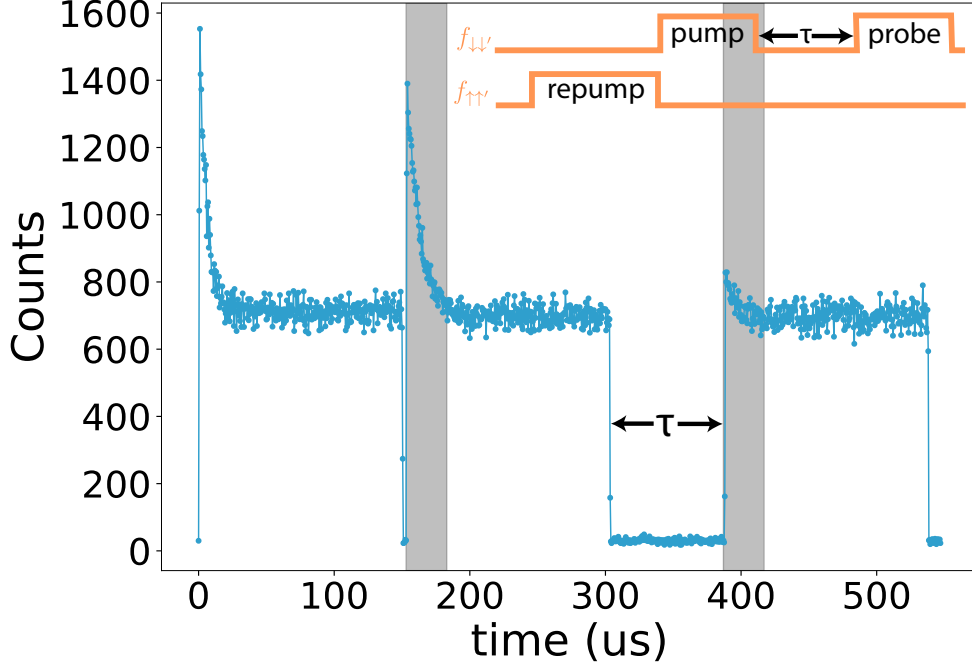


**Fig. 11** An example histogram of photon detection times collected from the inset optical pulse sequence and a particular value of  $\tau$ .

that initialization in the spin up state (blue data in Fig. 12) produces a greater contrast in the spin relaxation curve at long time delays (relative to  $1/\gamma_s$ ) when compared with initialization in the spin down state (red data in Fig. 12). The data is taken at a magnetic field magnitude of 1 kG and orientation of  $\theta \approx 55^\circ$ . The characteristic exponential timescale of spin relaxation for both cases is similar. At long time delays, the spin will relax to a thermal state. Based on the temperature of the SiV's environment,  $T$  and the energy difference between the spin qubit levels,  $\hbar\omega_s$  the steady-state population in the spin up and down states is given by the relations:

$$p_\uparrow(\tau \gg T_1) = \frac{1}{e^{\frac{\hbar\omega_s}{k_B T}} + 1} \quad (1)$$

$$p_\downarrow(\tau \gg T_1) = 1 - \frac{1}{e^{\frac{\hbar\omega_s}{k_B T}} + 1} \quad (2)$$

Our measurements yield an estimated SiV temperature of  $\sim 150$  mK in the steady state. This is elevated above the thermometer readings on the copper sample mount (65 mK) and the mixing plate thermometer (44 mK), likely due to residual optical probe heating [43]. Nonetheless, at this temperature of  $\sim 150$  mK, the 12 GHz mechanical breathing mode of our device is expected to be close to the ground state with an expected thermal phonon occupancy of 0.02 quanta. This temperature is also significantly below the temperature for  $> 99\%$  population in the lower orbital branch of

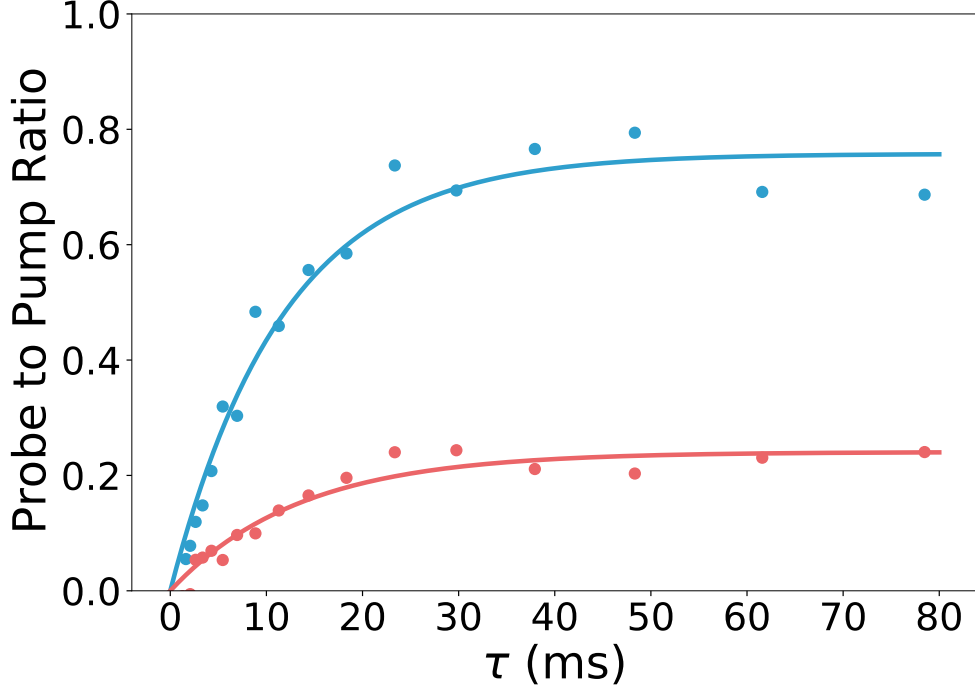


**Fig. 12** Example spin decay curves measured with a 1 kG magnetic field with  $\theta \approx 55^\circ$  (corresponding to a spin transition frequency of 2.8 GHz). Blue (red) curves measured with the pump/probe laser parked on the  $f_{\uparrow\uparrow}$  ( $f_{\downarrow\downarrow}$ ) transition.

the SiV ground state, calculated to be  $\sim 885$  mK, given  $\Delta_{GS} = 85$  GHz. Around this temperature, the phonon population resonant with the 85 GHz ground state orbital transition can act as an additional channel for spin relaxation via an Orbach process which can dominate the direct spin-relaxation pathway [12, 16].

Fig. 13 shows the temperature-dependent spin relaxation data measured by applying a controlled amount of heat to the mixing plate of the dilution fridge. As the mixing plate temperature is raised, the spin qubit is found to decay faster with a steady state ( $\tau \gg 1/\gamma_s$ ) population value tending towards 0.5 which corresponds to a completely mixed spin state. This behavior is expected at higher temperatures relative to the spin transition frequency. The SiV temperature estimate for each measurement can be extracted from the long-time population saturation value and is shown inset to Fig. 13. In the temperature range probed in these measurements, the SiV temperature estimate from this method is in good agreement with the temperature reading on the mixing plate thermometer.

## 5.9 Determination of Extrinsic Optical Cavity Loss Rate

It was observed that the quality factor and depth of resonance dip changed after the device was cleaned and cladded in ALD alumina. We suspect, but do not know, that

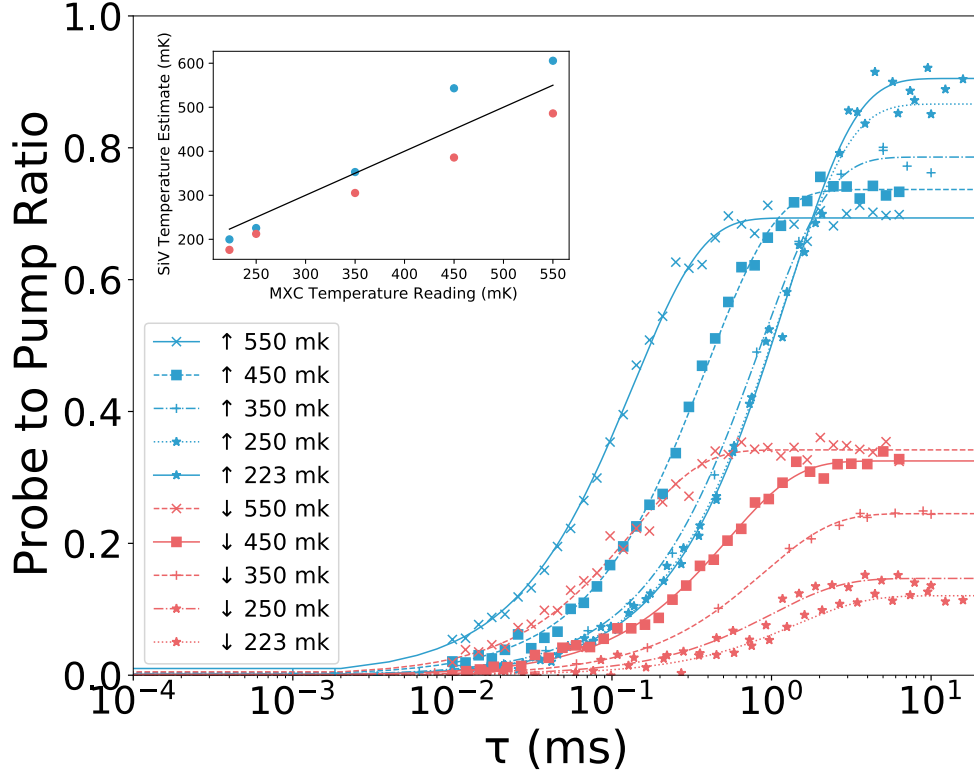


**Fig. 13** Temperature dependent spin decay curves. With an applied magnetic field of 3 kG aligned with the laboratory z-axis (corresponding to a spin transition frequency of 8.3 GHz), the spin decay is measured at five different elevated temperatures. Measurements are performed on both probe transitions while applying controlled heat to the mixing plate and keeping the optical probe powers constant. Using the steady state population, an SiV temperature estimate was extracted. The inset shows a plot of this estimated SiV temperature against the temperature recorded on the MXC thermometer of the dilution fridge.

the cleaning was the step responsible for the slight  $Q_o$  increase. Fits to both spectra assuming an undercoupled cavity yields  $\kappa_e \approx 4$  GHz. Fits assuming an overcoupled system do not yield consistent results for  $\kappa_e$  leading us to believe that our devices are undercoupled with  $\kappa_i \approx 11$  GHz and  $\kappa_e \approx 4$  GHz for the ALD alumina-cladded case. This is the best measurement of  $\kappa_e$  that we can make in the absence of cavity optical phase response measurements, which are difficult due to the relatively large optical linewidths of our device relative to the available bandwidth of visible-wavelength electro-optic modulators and photodetectors.

## 5.10 Angle-Dependent Spin Decay Spectra

In Fig. 4b we studied the effect of the magnetic field orientation on the spin decay rate spectrum of an example feature around 21 GHz, the details of the spectra are

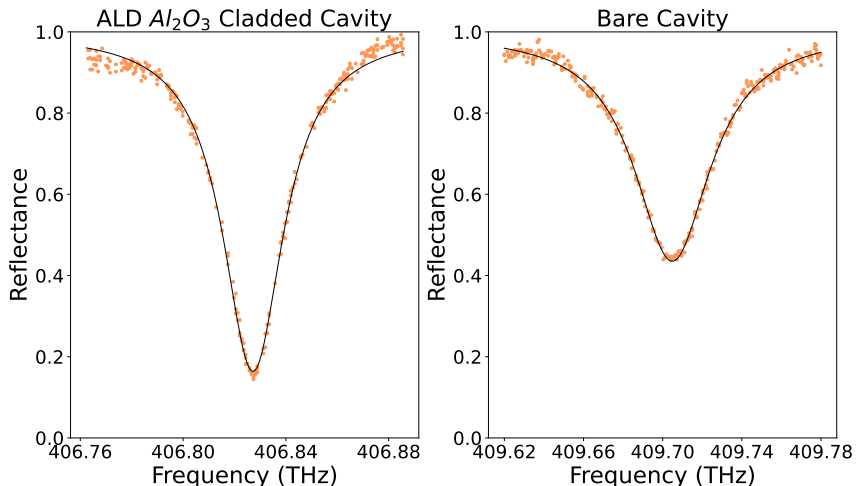


**Fig. 14** Optical reflectance measurement of the bare optical cavity and the cleaned and ALD alumina cladded cavity. The total optical decay rate is  $\sim 20$  GHz for the bare cavity and  $\sim 15$  GHz for the ALD alumina clad cavity.

shown here in Fig. 15. We chose to study this high frequency feature because at alignments close the SiV axis the splitting between  $f_{\uparrow\uparrow'}$  and  $f_{\downarrow\down'}$  is small, making it much easier to study high frequency modes. In Fig. 15 we sweep the spin transition frequency across this  $\sim 21$  GHz feature by adjusting the magnetic field magnitude for five different magnetic field orientations. The amplitude and baseline of the  $\sim 21$  GHz feature increase as the field alignment rotates from close to parallel with the SiV axis towards the perpendicular.

### 5.11 SEM Analysis of fabricated device

The goal of the OMC cavity design in this work is to achieve an optical/mechanical cavity mode pair which simultaneously enables optical readout of the SiV center's spin properties and optomechanical readout of the mechanical mode properties. This requires high values of  $\{g_{so}, g_{om}, g_{sm}\}$  and low values of  $\{\kappa_o, \kappa_m\}$ . There has been a great deal of previous work on designing mode pairs which satisfy these criteria.[63] We choose the fundamental TE-like optical mode, mechanical 'breathing mode' pair, which features a near-optimal photoelastic overlap integral between the optical  $E_y$  field component with the strain  $\epsilon_{YY}$  field component, which enables large optomechanical coupling. The TE-like optical mode also supports efficient spin-photon interactions and the mechanical breathing mode supports efficient spin-phonon interactions for an SiV oriented  $45^\circ$  relative to the beam.

The cavity region of the fabricated device is shown in Fig. 16. A unit cell design akin to the conventional elliptical hole shape is used (where the hole is defined by its major/minor axis lengths) except an additional parameter  $R$  is introduced, which determines the radius of curvature near the hole edge.

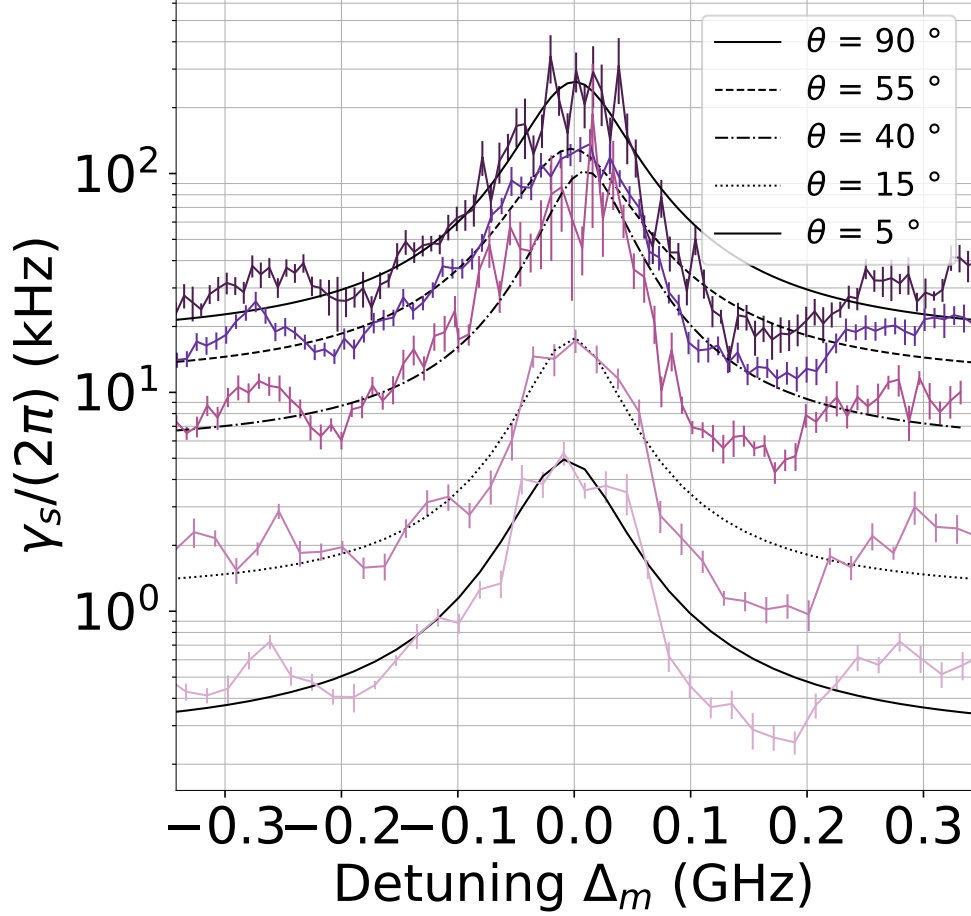


**Fig. 15** Spin decay rate spectra and fits at different magnetic field orientation relative to the axis of the SiV center for an example feature around 21 GHz.

To accurately compare the experimental results to simulation, we took detailed SEM images of each unit cell hole in the OMC. Image processing on the SEM images then extracts the fabricated unit cell parameters, with the addition of the parameter  $r_{\text{fil}}$  to account for rounding at the vertical extents of the unit cell hole. For the device under study, we observe the measured parameters in Table 1.

These parameters deviate from the nominal parameters of our device within normal fabrication tolerances, but do lead to measurable shifts in device properties. The simulation-based analyses in the following sections are performed using these fitted parameters.

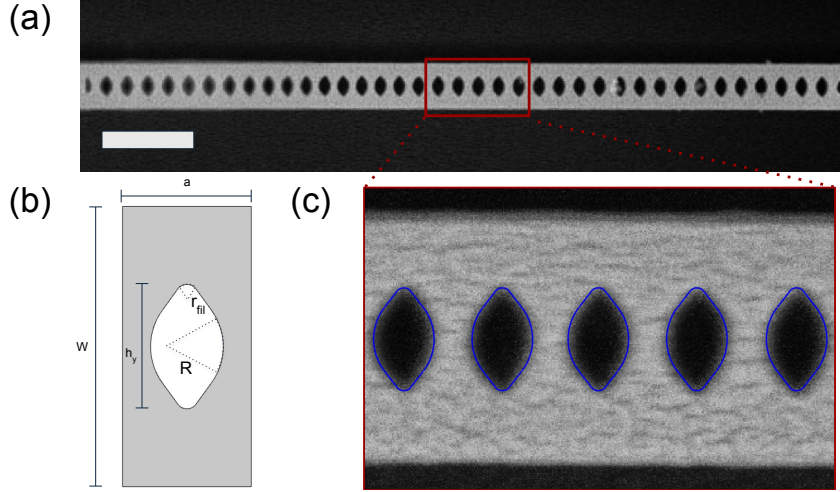


**Fig. 16** (a) SEM of the cavity region of the device studied in this work. (b) Parameterized diagram of the OMC cavity unit cell. (c) SEM of 5 unit cells in the OMC cavity with best fit unit cells drawn in blue.

Parameter	Measured Value	Designed Value
Beam thickness ( $th$ )	150 nm	160 nm
Beam width ( $w$ )	530 nm	540 nm
Radius ( $R$ )	110 nm	100 nm
Angle ( $\theta$ )	$36^\circ$	$36^\circ$
Hole height ( $h_y$ )	240 nm	236 nm
Fillet radius ( $r_{fil}$ )	30 nm	0 nm

**Table 1** Comparison of SEM and Nominal Parameter Values

## 5.12 Simulation of the optomechanical cavity

The optical TE-like and mechanical breathing modes were simulated using the geometric parameters obtained from SEM images. Fig 1(a) and Fig 1(b) show the simulated profiles of these modes. The masked implantation process embeds SiV centers within a 100 nm x 100 nm area (green square shown in Fig 17a and Fig 17b). The TE-like mode has a simulated wavelength of 736 nm and a quality factor of  $3.2 \times 10^4$ . The breathing mode has a simulated frequency of 12.29 GHz and a quality factor of  $2.4 \times 10^5$ . While the measured optical Q-factor is similar to the simulated quality factor, the measured mechanical Q-factor is much lower than the simulated value.

Finally, Fig. 17 shows the optomechanical coupling rate of the breathing mode (orange dot) as well as those of all simulated mechanical modes from 5 - 28 GHz, which covers the range of data measured as part of the spin  $T_1$  spectrum in Fig. 4. With the exception of modes around 12 GHz, nearly all modes display negligible optomechanical coupling to the TE-like mode due to the strict symmetry requirements for such coupling [63].

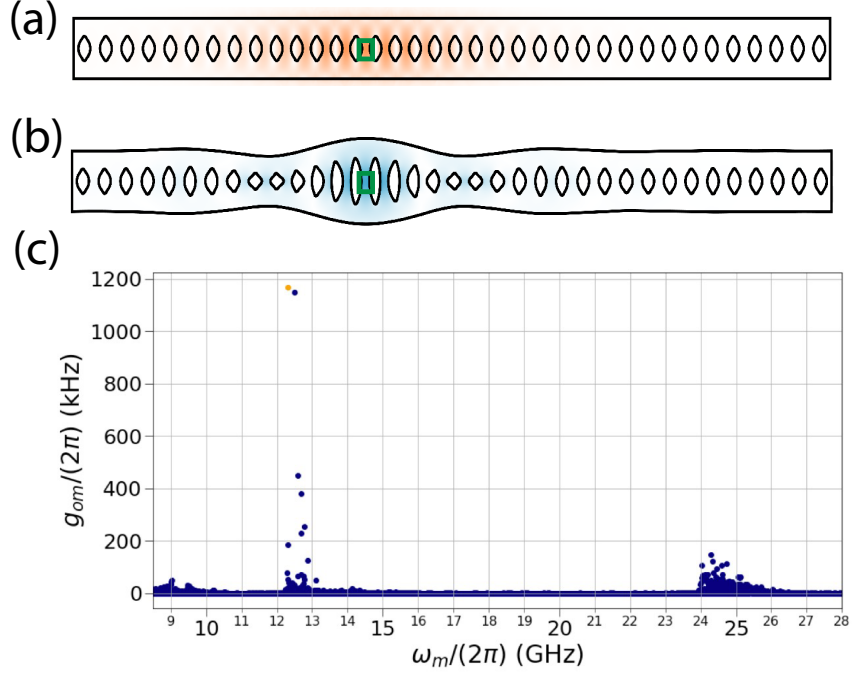


**Fig. 17** (a) Electric field profile of TE-like optical mode. Green box indicates masked implantation aperture, ensuring good alignment between E-field and SiV location which enables large spin-photon coupling. (b) Strain ( $\epsilon_{XX} + \epsilon_{YY} + \epsilon_{ZZ}$ ) profile of mechanical breathing mode. (c) Calculation of optomechanical coupling rate for full spectrum of mechanical eigenmodes. The orange dot signifies the breathing mode, showing that it satisfies the large  $g_{OM}$  requirement for optomechanical readout of the mechanical mode properties.

### 5.13 Simulation of spin-phonon coupling to the mechanical breathing mode

The strain profile of the breathing mode is used to calculate the strength of the spin-phonon coupling  $g_{sm}$  for an ideal zero static-strain SiV. Using perturbation theory [12, 64] the vacuum spin-phonon coupling rate  $g_{sm}$  is given by:

$$g_{sm} = \frac{2\gamma_s B_x}{\lambda_{SO,GS}} \sqrt{\beta^2 + \gamma^2} \quad (3)$$

where

$$\beta = d(\epsilon_{XX} - \epsilon_{YY}) + f\epsilon_{XZ} \quad (4)$$

$$\gamma = -2d\epsilon_{XY} + f\epsilon_{YZ} \quad (5)$$

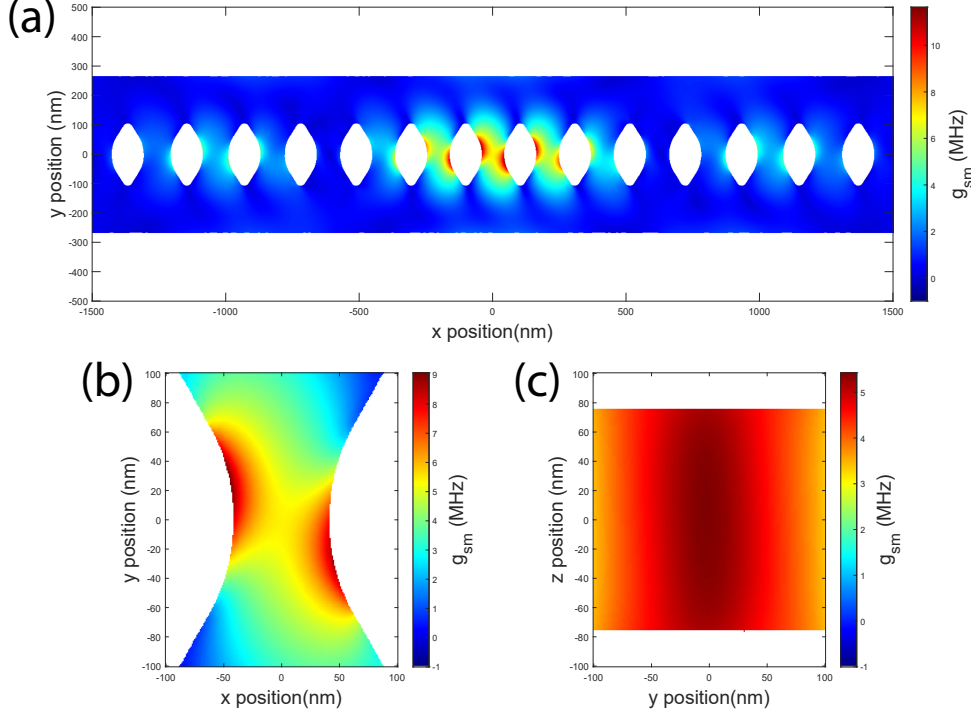


**Fig. 18** (a) XY slice plot of simulated  $g_{sm}$  in the cavity region. Large  $g_{sm}$  can be realized where strain is concentrated near the cavity center. (b) XY slice plot of simulated  $g_{sm}$  for the implantation aperture region.  $g_{sm}$  is sensitive to the in-plane location, with maximal  $g_{sm}$  found at the hole edges where strain is maximized. (c) YZ slice plot of simulated  $g_{sm}$  for the aperture region. The SiV centers are nominally implanted at the beam center ( $z=0$ ), but  $g_{sm}$  is insensitive to depth.

and the components of the static strain tensor  $\epsilon$  are in the coordinate frame of the SiV center.

With the exception of Fig 4b, Fig 7, and Fig 15, the data shown in this paper was taken using a magnetic field aligned to the z- axis in laboratory frame ( $\theta \approx 55^\circ$ ). In this case, the magnetic field component perpendicular to the SiV center's high-symmetry axis  $B_X$  is related to the spin transition frequency by  $\omega_s$  by equation  $\gamma_s B_X = \frac{\omega_s}{\sqrt{2}}$ , on resonance  $\omega_s = \omega_m$ .  $g_{sm}$  can then be expressed as:

$$g_{sm} = \frac{\sqrt{2}\omega_m}{\lambda_{SO}} \sqrt{(d(\epsilon_{XX} - \epsilon_{YY}) + f\epsilon_{YZ})^2 + (-2d\epsilon_{XY} + f\epsilon_{XZ})^2} \quad (6)$$

The SiV center's spin transition is sensitive to the strain transverse to its symmetry axis, precisely at the SiV center's location in the cavity. Large  $g_{sm}$  can be achieved in areas of maximal strain as seen in Fig 18 for the mechanical breathing mode of our OMC devices. Fig 18c shows that  $g_{sm}$  is largely insensitive to depth, but highly sensitive to in-plane location. Simulations suggest that under ideal conditions of low crystal strain (strain  $\ll \lambda_{so} = 46$  GHz in the orbital ground state) and a magnetic field

orientation perpendicular to the high-symmetry axis of the SiV [12],  $g_{sm}$  can reach a maximum value of 9 MHz. This is roughly a factor of 30 larger than the experimentally observed  $g_{sm}$ . This difference is well explained by the non-ideal conditions in our OMC devices, in particular the non-zero static crystal strain (5.2) and expected error in the SiV center's position with respect to the strain coupling maximum.

### 5.14 Simulation of spin-phonon coupling to the broadband acoustic density of states

While our design work focused on the mechanical breathing mode, the coupling of the SiV center to mechanical modes in the 8.5-28 GHz frequency range was measured and simulated as seen in Fig 19. To model the phonon-induced decay of the SiV center as a function of the spin transition frequency, we sum the contributions from all of these modes:

$$\Gamma(\omega) = 4 \sum_q \frac{g_q^2 \kappa_q}{\kappa_q^2 + 4(\omega_q - \omega)^2} \quad (7)$$

To account for the fact that the experimentally observed quality factor ( $Q_q = \frac{\omega_q}{\kappa_q}$ ) is lower than what is simulated, we include a phenomenological reduction in  $Q$  so that  $Q'_q = (Q_{sim}^{-1} + Q_{damp}^{-1})^{-1}$ , where  $Q_{damp} = 350$  based on the experimentally observed linewidth broadening of the breathing mode. We also account for the static-strain of the SiV as measured in section 5.2, which leads to a reduction in  $g_q$ .

The highly local nature of spin-phonon coupling poses a modelling challenge due to the uncertain position of the SiV center within the implantation aperture, which is 50 nm wide in both the x and y directions. As seen in Fig. 19, even a few nanometer change of the in-plane location of the SiV center results in qualitatively distinct spin decay spectra. Nonetheless, many of the experimentally observed features, are seen in our simulations. In particular, a resonance in the spin decay rate due to the 12 GHz breathing mode of the device can be observed consistently.

## References

- [1] Cohen-Tannoudji, C., Dupont-Roc, J., Grynberg, G.: Atom-Photon Interactions: Basic Processes and Applications. John Wiley & Sons, Hoboken, NJ, USA (1998)
- [2] Purcell, E.M., Torrey, H.C., Pound, R.V.: Resonance Absorption by Nuclear Magnetic Moments in a Solid. Physical Review **69**(1-2), 37–38 (1946) <https://doi.org/10.1103/PhysRev.69.37> . Publisher: American Physical Society. Accessed 2025-03-12
- [3] Purcell, E.M.: Spontaneous emission probabilities at radio frequencies. Physical Review **69**, 681 (1946)
- [4] Walther, H., Varcoe, B.T.H., Englert, B.-G., Becker, T.: Cavity quantum electrodynamics. Reports on Progress in Physics **69**(5), 1325 (2006) <https://doi.org/10.1088/0034-4885/69/5/R02> . Accessed 2025-03-12

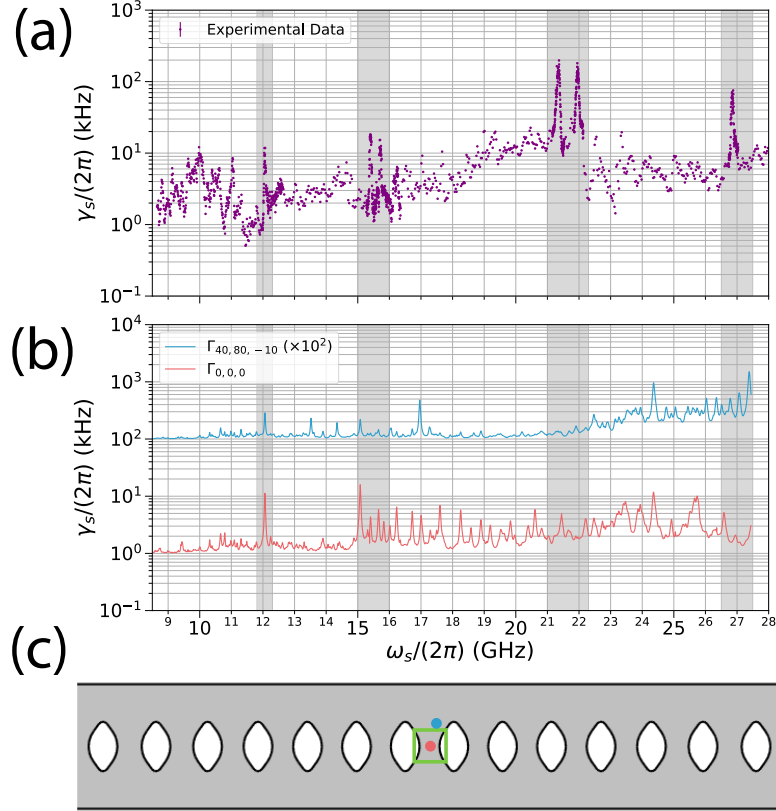


**Fig. 19** (a) Broadband spin decay spectrum for a  $\theta \approx 55^\circ$  magnetic field, also show in Fig. 4. Shaded regions indicate observed resonances of increased Purcell enhancement, attributed to localized mechanical modes. (b) Simulated spin decay spectrum  $\Gamma_{x,y,z}$  for different choices of SiV-center location relative to the cavity center (in nm). Note that some experimental features are reproduced (namely Purcell enhancement due to the  $\sim 12$  GHz breathing mode) for both locations, but qualitatively distinct features are observed at other frequencies. (c) Cavity diagram indicating the chosen points for simulation, the implantation aperture is shown in green.

- [5] Blais, A., Grimsmo, A.L., Girvin, S.M., Wallraff, A.: Circuit quantum electrodynamics. *Reviews of Modern Physics* **93**(2), 025005 (2021) <https://doi.org/10.1103/RevModPhys.93.025005> . Publisher: American Physical Society. Accessed 2025-03-12
- [6] Reiserer, A., Rempe, G.: Cavity-based quantum networks with single atoms and optical photons. *Reviews of Modern Physics* **87**(4), 1379–1418 (2015) <https://doi.org/10.1103/RevModPhys.87.1379> . Publisher: American Physical Society. Accessed 2025-03-12
- [7] Bienfait, A., Pla, J.J., Kubo, Y., Zhou, X., Stern, M., Lo, C.C., Weis, C.D., Schenkel, T., Vion, D., Esteve, D., Morton, J.J.L., Bertet, P.: Controlling spin relaxation with a cavity. *Nature* **531**(7592), 74–77 (2016) <https://doi.org/10.1038/531074a>

1038/nature16944 . Publisher: Nature Publishing Group. Accessed 2025-03-17

- [8] Nguyen, C.T., Sukachev, D.D., Bhaskar, M.K., Machielse, B., Levonian, D.S., Knall, E.N., Stroganov, P., Chia, C., Burek, M.J., Riedinger, R., Park, H., Lončar, M., Lukin, M.D.: An integrated nanophotonic quantum register based on silicon-vacancy spins in diamond. *Physical Review B* **100**(16), 165428 (2019) <https://doi.org/10.1103/PhysRevB.100.165428> . Publisher: American Physical Society. Accessed 2025-03-12
- [9] Bhaskar, M.K., Riedinger, R., Machielse, B., Levonian, D.S., Nguyen, C.T., Knall, E.N., Park, H., Englund, D., Lončar, M., Sukachev, D.D., Lukin, M.D.: Experimental demonstration of memory-enhanced quantum communication. *Nature* **580**(7801), 60–64 (2020) <https://doi.org/10.1038/s41586-020-2103-5> . Publisher: Nature Publishing Group. Accessed 2025-03-12
- [10] Uppu, R., Midolo, L., Zhou, X., Carolan, J., Lodahl, P.: Quantum-dot-based deterministic photon–emitter interfaces for scalable photonic quantum technology. *Nature Nanotechnology* **16**(12), 1308–1317 (2021) <https://doi.org/10.1038/s41565-021-00965-6> . Publisher: Nature Publishing Group. Accessed 2025-03-12
- [11] Kindem, J.M., Ruskuc, A., Bartholomew, J.G., Rochman, J., Huan, Y.Q., Faraon, A.: Control and single-shot readout of an ion embedded in a nanophotonic cavity. *Nature* **580**(7802), 201–204 (2020) <https://doi.org/10.1038/s41586-020-2160-9> . Publisher: Nature Publishing Group. Accessed 2025-03-12
- [12] Meesala, S., Sohn, Y.-I., Pingault, B., Shao, L., Atikian, H.A., Holzgrafe, J., Gündoğan, M., Stavrakas, C., Sipahigil, A., Chia, C., Evans, R., Burek, M.J., Zhang, M., Wu, L., Pacheco, J.L., Abraham, J., Bielejec, E., Lukin, M.D., Atatüre, M., Lončar, M.: Strain engineering of the silicon-vacancy center in diamond. *Physical Review B* **97**(20), 205444 (2018) <https://doi.org/10.1103/PhysRevB.97.205444> . Publisher: American Physical Society. Accessed 2025-03-12
- [13] Astner, T., Gugler, J., Angerer, A., Wald, S., Putz, S., Mauser, N.J., Trupke, M., Sumiya, H., Onoda, S., Isoya, J., Schmiedmayer, J., Mohn, P., Majer, J.: Solid-state electron spin lifetime limited by phononic vacuum modes. *Nature Materials* **17**(4), 313–317 (2018) <https://doi.org/10.1038/s41563-017-0008-y> . Publisher: Nature Publishing Group. Accessed 2025-03-12
- [14] Ahn, J., Wicker, C., Bitner, N., Solomon, M.T., Tissot, B., Burkard, G., Dibos, A.M., Zhang, J., Heremans, F.J., Awschalom, D.D.: Extended spin relaxation times of optically addressed vanadium defects in silicon carbide at telecommunication frequencies. *Physical Review Applied* **22**(4), 044078 (2024) <https://doi.org/10.1103/PhysRevApplied.22.044078> . Publisher: American Physical Society. Accessed 2025-03-12
- [15] Gilardoni, C.M., Bosma, T., Hien, D., Hendriks, F., Magnusson, B., Ellison, A.,

- Ivanov, I.G., Son, N.T., Wal, C.H.: Spin-relaxation times exceeding seconds for color centers with strong spin-orbit coupling in SiC. *New Journal of Physics* **22**(10), 103051 (2020) <https://doi.org/10.1088/1367-2630/abbf23> . Publisher: IOP Publishing. Accessed 2025-03-12
- [16] Orbach, R., Bleaney, B.: Spin-lattice relaxation in rare-earth salts. *Proceedings of the Royal Society of London. Series A. Mathematical and Physical Sciences* **264**(1319), 458–484 (1997) <https://doi.org/10.1098/rspa.1961.0211> . Publisher: Royal Society. Accessed 2025-03-12
- [17] Ruby, R.H., Benoit, H., Jeffries, C.D.: Paramagnetic resonance below 1k: Spin-lattice relaxation of ce<sup>3+</sup> and nd<sup>3+</sup> in lanthanum magnesium nitrate. *Physical Review* **127**(1), 51–65 (1962) <https://doi.org/10.1103/PhysRev.127.51>
- [18] Yang, Y., Kladarić, I., Drimmer, M., Lüpke, U., Lenterman, D., Bus, J., Marti, S., Fadel, M., Chu, Y.: A mechanical qubit. *Science* **386**(6723), 783–788 (2024) <https://doi.org/10.1126/science.adr2464> . Publisher: American Association for the Advancement of Science. Accessed 2025-03-12
- [19] Diamandi, H.H., Luo, Y., Mason, D., Kanmaz, T.B., Ghosh, S., Pavlovich, M., Yoon, T., Behunin, R., Puri, S., Harris, J.G.E., Rakich, P.T.: Quantum optomechanical control of long-lived bulk acoustic phonons. *arXiv. arXiv:2410.18037 [quant-ph]* (2024). <https://doi.org/10.48550/arXiv.2410.18037> . <http://arxiv.org/abs/2410.18037> Accessed 2025-03-12
- [20] MacCabe, G.S., Ren, H., Luo, J., Cohen, J.D., Zhou, H., Sipahigil, A., Mirhosseini, M., Painter, O.: Nano-acoustic resonator with ultralong phonon lifetime. *Science* **370**(6518), 840–843 (2020) <https://doi.org/10.1126/science.abc7312> . Publisher: American Association for the Advancement of Science. Accessed 2025-03-12
- [21] Bozkurt, A., Zhao, H., Joshi, C., LeDuc, H.G., Day, P.K., Mirhosseini, M.: A quantum electromechanical interface for long-lived phonons. *Nature Physics* **19**(9), 1326–1332 (2023) <https://doi.org/10.1038/s41567-023-02080-w> . Publisher: Nature Publishing Group. Accessed 2025-03-12
- [22] Wallucks, A., Marinković, I., Hensen, B., Stockill, R., Gröblacher, S.: A quantum memory at telecom wavelengths. *Nature Physics* **16**(7), 772–777 (2020) <https://doi.org/10.1038/s41567-020-0891-z> . Publisher: Nature Publishing Group. Accessed 2025-03-12
- [23] Manenti, R., Kockum, A.F., Patterson, A., Behrle, T., Rahamim, J., Tancredi, G., Nori, F., Leek, P.J.: Circuit quantum acoustodynamics with surface acoustic waves. *Nature Communications* **8**(1), 975 (2017) <https://doi.org/10.1038/s41467-017-01063-9> . Publisher: Nature Publishing Group. Accessed 2025-03-12
- [24] Meesala, S., Wood, S., Lake, D., Chiappina, P., Zhong, C., Beyer, A.D., Shaw,

- M.D., Jiang, L., Painter, O.: Non-classical microwave–optical photon pair generation with a chip-scale transducer. *Nature Physics* **20**(5), 871–877 (2024) <https://doi.org/10.1038/s41567-024-02409-z> . Publisher: Nature Publishing Group. Accessed 2025-03-12
- [25] Chu, Y., Gröblacher, S.: A perspective on hybrid quantum opto- and electromechanical systems. *Applied Physics Letters* **117**(15), 150503 (2020) <https://doi.org/10.1063/5.0021088> . Accessed 2025-03-12
- [26] Delaney, R.D., Urmey, M.D., Mittal, S., Brubaker, B.M., Kindem, J.M., Burns, P.S., Regal, C.A., Lehnert, K.W.: Superconducting-qubit readout via low-backaction electro-optic transduction. *Nature* **606**(7914), 489–493 (2022) <https://doi.org/10.1038/s41586-022-04720-2> . Publisher: Nature Publishing Group. Accessed 2025-03-12
- [27] Weaver, M.J., Duivesteyn, P., Bernasconi, A.C., Scharmer, S., Lemang, M., Thiel, T.C.v., Hijazi, F., Hensen, B., Gröblacher, S., Stockill, R.: An integrated microwave-to-optics interface for scalable quantum computing. *Nature Nanotechnology* **19**(2), 166–172 (2024) <https://doi.org/10.1038/s41565-023-01515-y> . Publisher: Nature Publishing Group. Accessed 2025-03-12
- [28] Ouartchaiyapong, P., Lee, K.W., Myers, B.A., Jayich, A.C.B.: Dynamic strain-mediated coupling of a single diamond spin to a mechanical resonator. *Nature Communications* **5**(1), 4429 (2014) <https://doi.org/10.1038/ncomms5429> . Publisher: Nature Publishing Group. Accessed 2025-03-12
- [29] Meesala, S., Sohn, Y.-I., Atikian, H.A., Kim, S., Burek, M.J., Choy, J.T., Lončar, M.: Enhanced Strain Coupling of Nitrogen-Vacancy Spins to Nanoscale Diamond Cantilevers. *Physical Review Applied* **5**(3), 034010 (2016) <https://doi.org/10.1103/PhysRevApplied.5.034010> . Publisher: American Physical Society. Accessed 2025-03-12
- [30] Teissier, J., Barfuss, A., Appel, P., Neu, E., Maletinsky, P.: Strain Coupling of a Nitrogen-Vacancy Center Spin to a Diamond Mechanical Oscillator. *Physical Review Letters* **113**(2), 020503 (2014) <https://doi.org/10.1103/PhysRevLett.113.020503> . Publisher: American Physical Society. Accessed 2025-03-12
- [31] MacQuarrie, E.R., Gosavi, T.A., Jungwirth, N.R., Bhave, S.A., Fuchs, G.D.: Mechanical Spin Control of Nitrogen-Vacancy Centers in Diamond. *Physical Review Letters* **111**(22), 227602 (2013) <https://doi.org/10.1103/PhysRevLett.111.227602> . Publisher: American Physical Society. Accessed 2025-03-12
- [32] Maity, S., Shao, L., Bogdanović, S., Meesala, S., Sohn, Y.-I., Sinclair, N., Pingault, B., Chalupnik, M., Chia, C., Zheng, L., Lai, K., Lončar, M.: Coherent acoustic control of a single silicon vacancy spin in diamond. *Nature Communications* **11**(1), 193 (2020) <https://doi.org/10.1038/s41467-019-13822-x> . Publisher: Nature Publishing Group. Accessed 2025-03-12

- [33] Maity, S., Pingault, B., Joe, G., Chalupnik, M., Assumpção, D., Cornell, E., Shao, L., Lončar, M.: Mechanical Control of a Single Nuclear Spin. *Physical Review X* **12**(1), 011056 (2022) <https://doi.org/10.1103/PhysRevX.12.011056> . Publisher: American Physical Society. Accessed 2025-03-12
- [34] Dietz, J.R., Jiang, B., Day, A.M., Bhave, S.A., Hu, E.L.: Spin-acoustic control of silicon vacancies in 4H silicon carbide. *Nature Electronics* **6**(10), 739–745 (2023) <https://doi.org/10.1038/s41928-023-01029-4> . Publisher: Nature Publishing Group. Accessed 2025-03-12
- [35] Whiteley, S.J., Wolfowicz, G., Anderson, C.P., Bourassa, A., Ma, H., Ye, M., Koolstra, G., Satzinger, K.J., Holt, M.V., Heremans, F.J., Cleland, A.N., Schuster, D.I., Galli, G., Awschalom, D.D.: Spin–phonon interactions in silicon carbide addressed by Gaussian acoustics. *Nature Physics* **15**(5), 490–495 (2019) <https://doi.org/10.1038/s41567-019-0420-0> . Publisher: Nature Publishing Group. Accessed 2025-03-12
- [36] Kuruma, K., Pingault, B., Chia, C., Haas, M., Joe, G.D., Assumpcao, D.R., Ding, S.W., Jin, C., Xin, C.J., Yeh, M., Sinclair, N., Lončar, M.: Controlling interactions between high-frequency phonons and single quantum systems using phononic crystals. *Nature Physics* **21**(1), 77–82 (2025) <https://doi.org/10.1038/s41567-024-02697-5> . Publisher: Nature Publishing Group. Accessed 2025-03-12
- [37] Eichenfield, M., Chan, J., Camacho, R.M., Vahala, K.J., Painter, O.: Optomechanical crystals. *Nature* **462**(7269), 78–82 (2009) <https://doi.org/10.1038/nature08524> . Publisher: Nature Publishing Group. Accessed 2025-03-12
- [38] Joe, G., Chia, C., Pingault, B., Haas, M., Chalupnik, M., Cornell, E., Kuruma, K., Machielse, B., Sinclair, N., Meesala, S., Lončar, M.: High Q-Factor Diamond Optomechanical Resonators with Silicon Vacancy Centers at Millikelvin Temperatures. *Nano Letters* **24**(23), 6831–6837 (2024) <https://doi.org/10.1021/acs.nanolett.3c04953> . Publisher: American Chemical Society. Accessed 2025-03-12
- [39] Hepp, C., Müller, T., Waselowski, V., Becker, J.N., Pingault, B., Sternschulte, H., Steinmüller-Nethl, D., Gali, A., Maze, J.R., Atatüre, M., Becher, C.: Electronic Structure of the Silicon Vacancy Color Center in Diamond. *Physical Review Letters* **112**(3), 036405 (2014) <https://doi.org/10.1103/PhysRevLett.112.036405> . Publisher: American Physical Society. Accessed 2025-03-12
- [40] Burek, M.J., Cohen, J.D., Meenehan, S.M., El-Sawah, N., Chia, C., Ruelle, T., Meesala, S., Rochman, J., Atikian, H.A., Markham, M., Twitchen, D.J., Lukin, M.D., Painter, O., Lončar, M.: Diamond optomechanical crystals. *Optica* **3**(12), 1404–1411 (2016) <https://doi.org/10.1364/OPTICA.3.001404> . Publisher: Optica Publishing Group. Accessed 2025-03-12

- [41] Li, X., Lekavicius, I., Noeckel, J., Wang, H.: Ultracoherent Gigahertz Diamond Spin-Mechanical Lamb Wave Resonators. *Nano Letters* **24**(35), 10995–11001 (2024) <https://doi.org/10.1021/acs.nanolett.4c03071> . Publisher: American Chemical Society. Accessed 2025-03-12
- [42] Sukachev, D.D., Sipahigil, A., Nguyen, C.T., Bhaskar, M.K., Evans, R.E., Jelezko, F., Lukin, M.D.: Silicon-Vacancy Spin Qubit in Diamond: A Quantum Memory Exceeding 10 ms with Single-Shot State Readout. *Physical Review Letters* **119**(22), 223602 (2017) <https://doi.org/10.1103/PhysRevLett.119.223602> . Publisher: American Physical Society. Accessed 2025-03-12
- [43] Knall, E.N., Knaut, C.M., Bekenstein, R., Assumpcao, D.R., Stroganov, P.L., Gong, W., Huan, Y.Q., Stas, P.-J., Machielse, B., Chalupnik, M., Levonian, D., Suleymanzade, A., Riedinger, R., Park, H., Lončar, M., Bhaskar, M.K., Lukin, M.D.: Efficient Source of Shaped Single Photons Based on an Integrated Diamond Nanophotonic System. *Physical Review Letters* **129**(5), 053603 (2022) <https://doi.org/10.1103/PhysRevLett.129.053603> . Publisher: American Physical Society. Accessed 2025-03-12
- [44] Burek, M.J., Meuwly, C., Evans, R.E., Bhaskar, M.K., Sipahigil, A., Meesala, S., Machielse, B., Sukachev, D.D., Nguyen, C.T., Pacheco, J.L., Bielejec, E., Lukin, M.D., Lončar, M.: Fiber-Coupled Diamond Quantum Nanophotonic Interface. *Physical Review Applied* **8**(2), 024026 (2017) <https://doi.org/10.1103/PhysRevApplied.8.024026> . Publisher: American Physical Society. Accessed 2025-03-12
- [45] Khanaliloo, B., Mitchell, M., Hryciw, A.C., Barclay, P.E.: High-Q/V Monolithic Diamond Microdisks Fabricated with Quasi-isotropic Etching. *Nano Letters* **15**(8), 5131–5136 (2015) <https://doi.org/10.1021/acs.nanolett.5b01346> . Publisher: American Chemical Society. Accessed 2025-03-20
- [46] Evans, R.E., Bhaskar, M.K., Sukachev, D.D., Nguyen, C.T., Sipahigil, A., Burek, M.J., Machielse, B., Zhang, G.H., Zibrov, A.S., Bielejec, E., Park, H., Lončar, M., Lukin, M.D.: Photon-mediated interactions between quantum emitters in a diamond nanocavity. *Science* **362**(6415), 662–665 (2018) <https://doi.org/10.1126/science.aau4691> . Publisher: American Association for the Advancement of Science. Accessed 2025-03-12
- [47] Aspelmeyer, M., Kippenberg, T.J., Marquardt, F.: Cavity optomechanics. *Reviews of Modern Physics* **86**(4), 1391–1452 (2014) <https://doi.org/10.1103/RevModPhys.86.1391> . Publisher: American Physical Society. Accessed 2025-03-12
- [48] Waks, E., Vuckovic, J.: Dipole Induced Transparency in Drop-Filter Cavity-Waveguide Systems. *Physical Review Letters* **96**(15), 153601 (2006) <https://doi.org/10.1103/PhysRevLett.96.153601> . Publisher: American Physical Society. Accessed 2025-03-12

- [49] Sipahigil, A., Evans, R.E., Sukachev, D.D., Burek, M.J., Borregaard, J., Bhaskar, M.K., Nguyen, C.T., Pacheco, J.L., Atikian, H.A., Meuwly, C., Camacho, R.M., Jelezko, F., Bielejec, E., Park, H., Lončar, M., Lukin, M.D.: An integrated diamond nanophotonics platform for quantum-optical networks. *Science* **354**(6314), 847–850 (2016) <https://doi.org/10.1126/science.aah6875> . Publisher: American Association for the Advancement of Science. Accessed 2025-03-12
- [50] Pederson, R.C., Miller, C.D., Arvidson, J.M., Blount, K., Schulze, M.: Problems involved in determining the mechanical properties of solid nitrogen and a composite of solid nitrogen and aluminum foam (40 k – 61 k). *Springer* **44**, 339–347 (1998) [https://doi.org/10.1007/978-1-4757-9056-6\\_45](https://doi.org/10.1007/978-1-4757-9056-6_45)
- [51] Perahia, R., Cohen, J.D., Meenehan, S., Alegre, T.P.M., Painter, O.: Electrostatically tunable optomechanical “zipper” cavity laser. *Applied Physics Letters* **97**(19), 191112 (2010) <https://doi.org/10.1063/1.3515296> . Accessed 2025-03-12
- [52] Jiang, W., Sarabalis, C.J., Dahmani, Y.D., Patel, R.N., Mayor, F.M., McKenna, T.P., Van Laer, R., Safavi-Naeini, A.H.: Efficient bidirectional piezo-optomechanical transduction between microwave and optical frequency. *Nature Communications* **11**(1), 1166 (2020) <https://doi.org/10.1038/s41467-020-14863-3> . Publisher: Nature Publishing Group. Accessed 2025-03-12
- [53] Neuman, T., Eichenfield, M., Trusheim, M.E., Hackett, L., Narang, P., Englund, D.: A phononic interface between a superconducting quantum processor and quantum networked spin memories. *npj Quantum Information* **7**(1), 121 (2021) <https://doi.org/10.1038/s41534-021-00457-4>
- [54] Covey, J.P., Weinfurter, H., Bernien, H.: Quantum networks with neutral atom processing nodes. *npj Quantum Information* **9**(1), 1–12 (2023) <https://doi.org/10.1038/s41534-023-00759-9> . Publisher: Nature Publishing Group. Accessed 2025-03-13
- [55] Monroe, C., Raussendorf, R., Ruthven, A., Brown, K.R., Maunz, P., Duan, L.-M., Kim, J.: Large-scale modular quantum-computer architecture with atomic memory and photonic interconnects. *Physical Review A* **89**(2), 022317 (2014) <https://doi.org/10.1103/PhysRevA.89.022317> . Publisher: American Physical Society. Accessed 2025-03-13
- [56] Schütz, M.J.A.: *Universal Quantum Transducers Based on Surface Acoustic Waves*. Springer International Publishing, 143–196 (2017) [https://doi.org/10.1007/978-3-319-48559-1\\_4](https://doi.org/10.1007/978-3-319-48559-1_4) . Accessed 2025-03-13
- [57] Lemonde, M.-A., Meesala, S., Sipahigil, A., Schuetz, M.J.A., Lukin, M.D., Loncar, M., Rabl, P.: Phonon Networks with Silicon-Vacancy Centers in Diamond Waveguides. *Physical Review Letters* **120**(21), 213603 (2018) <https://doi.org/10.1103/PhysRevLett.120.213603> . Publisher: American Physical Society. Accessed 2025-03-13

- [58] Chen, M., Owens, J.C., Putterman, H., Schäfer, M., Painter, O.: Phonon engineering of atomic-scale defects in superconducting quantum circuits. *Science Advances* **10**(37), 6240 (2024) <https://doi.org/10.1126/sciadv.ado6240> . Publisher: American Association for the Advancement of Science. Accessed 2025-03-13
- [59] Maksymowych, M.P., Yuksel, M., Hitchcock, O.A., Lee, N.R., Mayor, F.M., Jiang, W., Roukes, M.L., Safavi-Naeini, A.H.: Frequency Fluctuations in Nanomechanical Resonators due to Quantum Defects. arXiv. arXiv:2501.08289 [cond-mat] (2025). <https://doi.org/10.48550/arXiv.2501.08289> . <http://arxiv.org/abs/2501.08289> Accessed 2025-03-13
- [60] Yuksel, M., Maksymowych, M.P., Hitchcock, O.A., Mayor, F.M., Lee, N.R., Dykman, M.I., Safavi-Naeini, A.H., Roukes, M.L.: Strong Coupling of Nanomechanical Vibrations to Individual Two-Level Systems. arXiv. arXiv:2502.18587 [cond-mat] (2025). <https://doi.org/10.48550/arXiv.2502.18587> . <http://arxiv.org/abs/2502.18587> Accessed 2025-03-13
- [61] Kuruma, K., Pingault, B., Chia, C., Renaud, D., Hoffmann, P., Iwamoto, S., Ronning, C., Lončar, M.: Coupling of a single tin-vacancy center to a photonic crystal cavity in diamond. *Applied Physics Letters* **118**(23), 230601 (2021) <https://doi.org/10.1063/5.0051675> . Accessed 2025-03-13
- [62] Machielse, B., Bogdanovic, S., Meesala, S., Gauthier, S., Burek, M.J., Joe, G., Chalupnik, M., Sohn, Y.I., Holzgrafe, J., Evans, R.E., Chia, C., Atikian, H., Bhaskar, M.K., Sukachev, D.D., Shao, L., Maity, S., Lukin, M.D., Lončar, M.: Quantum Interference of Electromechanically Stabilized Emitters in Nanophotonic Devices. *Physical Review X* **9**(3), 031022 (2019) <https://doi.org/10.1103/PhysRevX.9.031022> . Publisher: American Physical Society. Accessed 2025-03-13
- [63] Chan, J., Safavi-Naeini, A.H., Hill, J.T., Meenehan, S., Painter, O.: Optimized optomechanical crystal cavity with acoustic radiation shield. *Applied Physics Letters* **101**(8), 081115 (2012) <https://doi.org/10.1063/1.4747726> . Accessed 2025-03-13
- [64] Chia, C.: Quantum optomechanics with color centers in diamond. PhD thesis, Harvard University Graduate School of Arts and Sciences, Cambridge, MA (May 2021). Doctoral dissertation. <https://nrs.harvard.edu/URN-3:HUL.INSTREPOS:37368314>